

## LORD OF THE RINGS: A KINEMATIC DISTANCE TO CIRCINUS X-1 FROM A GIANT X-RAY LIGHT ECHO

S. HEINZ<sup>1</sup>, M. BURTON<sup>2</sup>, C. BRAIDING<sup>2</sup>, W. N. BRANDT<sup>3,4,5</sup>, P. G. JONKER<sup>6,7,8</sup>, P. SELL<sup>9</sup>,  
R. P. FENDER<sup>10</sup>, M. A. NOWAK<sup>11</sup>, AND N. S. SCHULZ<sup>11</sup><sup>1</sup> Department of Astronomy, University of Wisconsin-Madison, Madison, WI 53706, USA; heinzs@astro.wisc.edu<sup>2</sup> School of Physics, University of New South Wales, Sydney, NSW 2052, Australia<sup>3</sup> Department of Astronomy & Astrophysics, The Pennsylvania State University, University Park, PA 16802, USA<sup>4</sup> Institute for Gravitation and the Cosmos, The Pennsylvania State University, University Park, PA 16802, USA<sup>5</sup> Department of Physics, The Pennsylvania State University, University Park, PA 16802, USA<sup>6</sup> SRON, Netherlands Institute for Space Research, 3584 CA, Utrecht, The Netherlands<sup>7</sup> Department of Astrophysics/IMAPP, Radboud University Nijmegen, 6500 GL, Nijmegen, The Netherlands<sup>8</sup> Harvard-Smithsonian Center for Astrophysics, Cambridge, MA 02138, USA<sup>9</sup> Physics Department, Texas Technical University, Lubbock, TX 79409, USA<sup>10</sup> Department of Astronomy, University of Oxford, Astrophysics, Oxford OX1 3RH, UK<sup>11</sup> Kavli Institute for Astrophysics and Space Research, Massachusetts Institute of Technology, Cambridge, MA 02139, USA

Received 2015 February 15; accepted 2015 May 14; published 2015 June 23

## ABSTRACT

Circinus X-1 exhibited a bright X-ray flare in late 2013. Follow-up observations with *Chandra* and *XMM-Newton* from 40 to 80 days after the flare reveal a bright X-ray light echo in the form of four well-defined rings with radii from 5 to 13 arcmin, growing in radius with time. The large fluence of the flare and the large column density of interstellar dust toward Circinus X-1 make this the largest and brightest set of rings from an X-ray light echo observed to date. By deconvolving the radial intensity profile of the echo with the MAXI X-ray light curve of the flare we reconstruct the dust distribution toward Circinus X-1 into four distinct dust concentrations. By comparing the peak in scattering intensity with the peak intensity in CO maps of molecular clouds from the Mopra Southern Galactic Plane CO Survey we identify the two innermost rings with clouds at radial velocity  $\sim -74$  and  $\sim -81$  km s<sup>-1</sup>, respectively. We identify a prominent band of foreground photoelectric absorption with a lane of CO gas at  $\sim -32$  km s<sup>-1</sup>. From the association of the rings with individual CO clouds we determine the kinematic distance to Circinus X-1 to be  $D_{\text{CirX-1}} = 9.4_{-1.0}^{+0.8}$  kpc. This distance rules out earlier claims of a distance around 4 kpc, implies that Circinus X-1 is a frequent super-Eddington source, and places a lower limit of  $\Gamma \gtrsim 22$  on the Lorentz factor and an upper limit of  $\theta_{\text{jet}} \lesssim 3^\circ$  on the jet viewing angle.

*Key words:* dust, extinction – stars: distances – stars: individual (Circinus X-1) – stars: neutron – techniques: radial velocities – X-rays: binaries

## 1. INTRODUCTION

## 1.1. X-Ray Dust Scattering Light Echoes

X-rays from bright point sources are affected by scattering off interstellar dust grains as they travel toward the observer. For sufficiently large dust column densities, a significant fraction of the flux can be scattered into an arcminute-sized, soft X-ray halo. Dust scattering halos have long been used to study the properties of the interstellar medium and, in some cases, to constrain the properties of the X-ray source (e.g., Mathis & Lee 1991; Predehl & Schmitt 1995; Corrales & Paerels 2013).

When the X-ray source is variable, the observable time-delay experienced by the scattered X-ray photons relative to the unscattered X-rays can provide an even more powerful probe of the ISM than a constant X-ray halo. In this case, the dust scattering halo will show temporal variations in intensity that can be cross-correlated with the light curve to constrain, for example, the distance to the dust clouds along the line of sight (e.g., Xiang et al. 2011).

A special situation arises when the X-ray source exhibits a strong and temporally well-defined flare (as observed, for example, in gamma-ray bursts (GRBs) and magnetars). In this case, the scattered X-ray signal is not a temporal and spatial average of the source flux history and the Galactic dust distribution, but a well-defined light echo in the form of distinct

rings of X-rays that increase in radius as time passes, given the longer and longer time delays (Vianello et al. 2007).

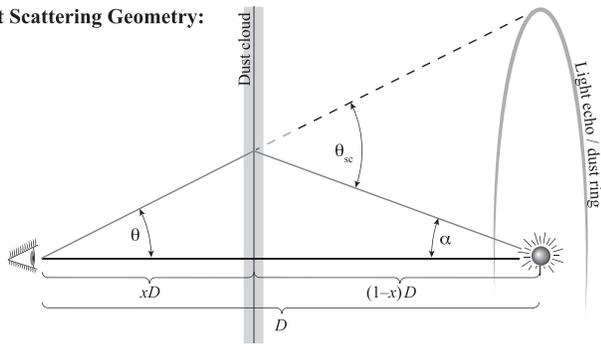
The scattering geometry of X-rays reflected by an interstellar dust cloud is illustrated in Figure 1. For a source distance  $D$  and a layer of interstellar dust at distance  $xD$  from the observer (such that the fractional distance to the dust layer is  $x$ ), the scattered X-rays must travel an additional distance  $\Delta D$ , which depends on the observed off-axis angle  $\theta$  (e.g., Mathis & Lee 1991; Xiang et al. 2011):

$$\Delta D = xD \left( \frac{1}{\cos(\theta)} - 1 \right) + (1-x)D \left( \frac{1}{\cos(\alpha)} - 1 \right) \\ \approx \frac{x D \theta^2 + (1-x) D \alpha^2}{2} = \frac{x D \theta^2}{2(1-x)}, \quad (1)$$

where we have used the small-angle approximation. The scattered signal will arrive with a time delay of

$$\Delta t = \frac{\Delta D}{c} = \frac{x D \theta^2}{2c(1-x)}. \quad (2)$$

For a well-defined (short) flare of X-rays, the scattered flare signal propagates outward from the source in an annulus of

**Dust Scattering Geometry:**


**Figure 1.** Cartoon of dust scattering geometry and nomenclature used throughout this paper. X-rays from a source at distance  $D$  scatter off a single dust layer at distance  $xD$  (such that the fractional distance is  $x$ ). The observed angle of the scattered X-rays is  $\theta$ , while the true scattering angle is  $\theta_{sc} = \theta + \alpha$ . The scattered X-rays travel an additional path length of  $\Delta D = \Delta D_1 + \Delta D_2$ .

angle

$$\theta = \sqrt{\frac{2c\Delta t(1-x)}{xD}}. \quad (3)$$

For a point source X-ray flux  $F(t)$  scattered by a thin sheet of dust of column density  $N_H$ , the X-ray intensity  $I_\nu$  of the dust scattering annulus at angle  $\theta$  observed at time  $t_{obs}$  is given by (Mathis & Lee 1991)

$$I_\nu(\theta, t_{obs}) = N_H \frac{F_\nu(t_{obs} - \Delta t_\theta)}{(1-x)^2} \frac{d\sigma_\nu}{d\Omega}, \quad (4)$$

where  $\Delta t_\theta$  is given by Equation (2) and  $d\sigma_\nu/d\Omega$  is the differential dust scattering cross section per hydrogen atom, integrated over the grain size distribution (e.g., Mathis & Lee 1991; Draine 2003). In the following, we will refer to the quantity  $N_H d\sigma_\nu/d\Omega$  as the dust scattering depth.

For a flare of finite duration scattering off a dust layer of finite thickness, the scattered signal will consist of a set of rings that reflect the different delay times for the different parts of the light curve relative to the time of the observation and the distribution of dust along the line of sight.<sup>12</sup>

In the presence of multiple well-defined scattering layers at different fractional distances  $x$  (with thickness  $l_{dust} \ll D$ ), each layer will generate a separate set of annuli. At a given time delay, the annuli of a fixed, short segment of the light curve are defined by the intersections of an ellipsoid of constant path length and each scattering layer. The superposition of the annuli from all dust layers (clouds) and the different parts of the flare light curve will create a set of (partially overlapping) rings. This situation is illustrated in Figure 2.

If the light curve of the X-ray flare that created the echo is known, an X-ray image of such a set of light-echo rings with sufficiently high angular resolution and signal-to-noise may be de-composed into contributions from a set of distinct dust layers at different distances. Such observations require both high angular resolution and sufficiently large collecting area and low background to detect the rings. The *Chandra* X-ray observatory is ideally suited for such observations.

<sup>12</sup> Because we will discuss delay times of several months, the much shorter duration of the X-ray observations may be neglected in the following discussion.

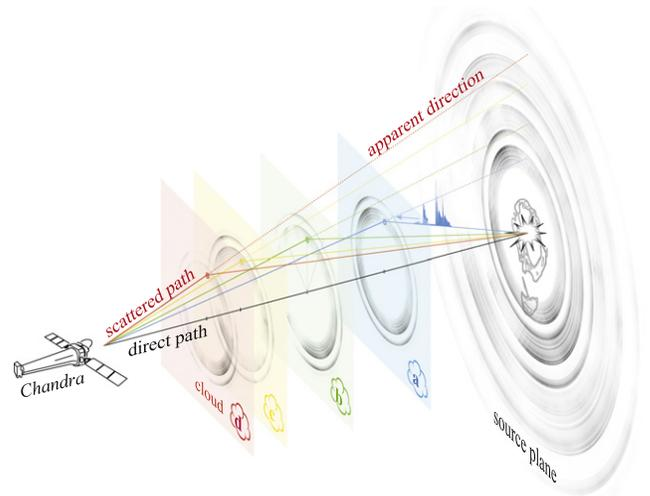


**Figure 2.** Cartoon of the X-ray dust-scattering echo analyzed in this paper: a bright flare from a point source (center of the source plane) propagates toward the observer. Dust in dense interstellar clouds between observer and source scatters X-rays toward the observer, producing a light echo in the form of well-defined rings. In this example, four clouds [a]–[d] shown in blue, green, yellow, and red, are located at different distances, illuminated by a bright flare (blue light curve) and producing four well-defined rings in the image/source plane.

## 1.2. Dust Echoes of Galactic X-Ray Sources

X-ray rings generated by dust scattering light echoes are extremely rare. To date, rings have been reported from five GRBs (Vianello et al. 2007, and references therein). For Galactic X-ray sources, observations of light echoes have been even more elusive. The soft gamma-ray repeater 1E 1547.0-5408 was the first Galactic X-ray source to show a clear set of bright X-ray light echo rings (Tiengo et al. 2010). Two other sources have also been reported to show light echo rings: the soft gamma-ray repeater SGR 1806-20 (Svirski et al. 2011) and the fast X-ray transient IGR J17544-2619 (Mao et al. 2014). However, the fluence of the initial X-ray flare in the latter two cases was too low to produce clearly resolved, arcminute-scale rings and both detections are tentative. In addition, McColough et al. (2013) found repeated scattering echoes from a single ISM cloud toward Cygnus X-3.

In the case of GRBs, the source is known to be at cosmological distances, which makes the scattering geometry particularly simple, since the source is effectively at infinite distance and the scattering angle is equal to the observed ring angle on the sky, which simplifies Equation (3) to

$$\theta_{\text{GRBecho}} = \sqrt{\frac{2c\Delta t}{D_{\text{dust}}}}. \quad (5)$$

An observed ring radius  $\theta_{\text{GRBecho}}$  and delay time  $\Delta t$  therefore unambiguously determine the distance to the dust.

However, in the case of Galactic sources, Equation (3) for  $\theta(\Delta t, D, x)$  cannot be inverted to solve for the distance to either the dust or the source individually, unless the distance to either the source or the dust is known a priori. If a particular ring can be identified with a dust cloud of known distance  $xD$ , the distance to the source can be determined from the known delay time  $\Delta t$ .

### 1.3. *Circinus X-1*

*Circinus X-1* is a highly variable X-ray binary that has often been characterized as erratic. It has been difficult to classify in terms of canonical X-ray binary schemes, combining properties of young and old X-ray binaries (Stewart et al. 1991; Oosterbroek et al. 1995; Jonker et al. 2007; Calvelo et al. 2012). The presence of type I X-ray bursts (Tennant et al. 1986; Linares et al. 2010) identifies the compact object in the source as a neutron star with a low magnetic field, supported by the presence of jets and the lack of X-ray or radio pulses (Stewart et al. 1993; Fender et al. 2004a; Tudose et al. 2006; Heinz et al. 2007; Soleri et al. 2009; Sell et al. 2010).

The transient nature and the low magnetic field suggested a classification of *Circinus X-1* as an old, low-mass X-ray binary with an evolved companion star (e.g., Shirey et al. 1996). This interpretation was in conflict with the observed orbital evolution time of order  $P/\dot{P} \sim 3000$  years (Parkinson et al. 2003; Clarkson et al. 2004) to  $P/\dot{P} \sim 20,000$  years (Nicolson 2007) and the possible identification of an A-B type super-giant companion star (Jonker et al. 2007), suggesting a much younger system age and a likely massive companion star. The orbital period of the system is 16.5 days, with a likely eccentricity around 0.45 (Jonker et al. 2007).

The conflicting identifications were resolved with the discovery of an arcminute scale supernova remnant in both X-ray and radio observations (Heinz et al. 2013), placing an upper limit of  $\tau < 4600$  years ( $D_{\text{Cir}}/8$  kpc) on the age of the system, where  $D_{\text{Cir}}$  is the distance to the source. This upper limit makes *Circinus X-1* the youngest known X-ray binary and an important test case for the study of both neutron star formation and orbital evolution in X-ray binaries.

The distance to *Circinus X-1* is highly uncertain. As a southern source deeply embedded in the Galactic disk, most standard methods of distance determination are not available. It is also out of the range of very long baseline interferometry (VLBI) parallax measurements. Distance estimates to *Circinus X-1* range from 4 kpc (Iaria et al. 2005) to 11 kpc (Stewart et al. 1991). A likely range of  $D = 8\text{--}10.5$  kpc was proposed by Jonker & Nelemans (2004) based on the radius-expansion burst method, using properties of the observed type I X-ray bursts. Because important binary properties depend on the distance to the source (such as the Eddington fraction of the source in outburst), a more accurate determination of the distance is critical for a more complete understanding of this important source.

*Circinus X-1* is a highly variable source, spanning over four orders of magnitude in luminosity from its quiescent flux to its brightest flares. While the source was consistently bright during the 1990s, it underwent a secular decline in flux starting in about 2000 and has spent the past 10 years below the detection thresholds of the *Rossi X-ray Timing Explorer* All Sky Monitor and the MAXI all sky monitor aboard the *International Space Station* (Matsuoka et al. 2009),<sup>13</sup> with the exception of sporadic near-Eddington flares, sometimes in excess of one Crab in flux (throughout the paper we will refer to the Eddington limit of  $L_{\text{Edd,NS}} \sim 1.8 \times 10^{38}$  erg s<sup>-1</sup> for a  $1.4 M_{\odot}$  neutron star). These flares typically occur within individual

binary orbits and are characterized by very rapid rises in flux near periastron of the binary orbit and often rapid flux decays at the end of the orbit. For example, during the five years it has been monitored by MAXI, *Circinus X-1* exhibited ten binary orbits with peak 2–10 keV fluxes in excess of  $\sim 10^{-8}$  erg cm<sup>-2</sup> s<sup>-1</sup> and five orbits with peak flux at or above one Crab.

The large dynamic range of the source flux, the well-defined duration of the X-ray flares, and the low mean flux during the quiescent periods over the past decades make *Circinus X-1* an ideal source for observations of X-ray light echoes. The source is located in the Galactic plane, at Galactic coordinates  $l = 322^{\circ}12$ ,  $b = 0^{\circ}04$ . The large neutral hydrogen column density of  $N_{\text{H}} \sim 2 \times 10^{22}$  cm<sup>-2</sup>, inferred from photoelectric absorption of the X-ray spectra of both the neutron star (e.g., Brandt & Schulz 2000) and the supernova remnant (Heinz et al. 2013), further increases the likelihood to observe light echoes.

In late 2013, *Circinus X-1* underwent an extremely bright flare, preceded and followed by long periods of very low X-ray flux. In this paper, we report the detection of the brightest and largest set of X-ray dust scattering rings observed to date, generated by the light echo from the 2013 flare. The spatial variation of the rings allows us to identify the interstellar clouds responsible for the different rings, which determines the distance to the X-ray source, *Circinus X-1*, to roughly 10% accuracy.

We will describe the observations and data analysis in Section 2. Section 3 describes the analysis of the X-ray, CO, and H I data and the procedure for deconvolving the X-ray signal into the line of sight dust distribution. In Section 4, we derive a new distance to *Circinus X-1* and discuss the consequences for the physics of this unique X-ray binary and for the physics of dust scattering. Section 5 briefly summarizes our findings.

## 2. OBSERVATIONS AND DATA REDUCTION

### 2.1. X-Ray Observations

*Circinus X-1* was observed with *Chandra*, *XMM-Newton*, and *Swift* in early 2014 after a bright X-ray flare of the source in late 2013. Figure 3 shows the time of the *Chandra* and *XMM-Newton* observations overlaid on the MAXI light curve of the source. The source exhibited a bright flare during three binary orbits approximately 50–100 days before the first *Chandra* observation (Asai et al. 2014), with a quiescent binary orbit interspersed during the first half of the flare. The source flare reached fluxes in excess of one Crab, with a total 2–4 keV fluence of  $\mathcal{F}_{2-4} = 0.025$  erg cm<sup>-2</sup>. The light curve of the flare has three characteristic peaks and a pronounced gap. This is the most energetic flare *Circinus X-1* has exhibited since it entered its long-term quiescent state in 2006, and is comparable in peak flux to the brightest flares the source has undergone even during its long-term outburst.

Before and during the *Chandra* campaign, *Swift* observed the source 12 times for a total exposure of 12 ks in order to safely schedule the *Chandra* observations. The history of bright flares by *Circinus X-1*, which can exceed the ACIS dose limit even during moderate exposures presents a significant scheduling challenge, and frequent monitoring of the source with *Swift* was used to confirm that the source was safely below the maximum flux allowable under *Chandra* instrument safety

<sup>13</sup> The ASM was one of three instruments aboard the *Rossi X-ray Timing Explorer*; MAXI is an experiment aboard the *International Space Station*; both have only one mode of operation.

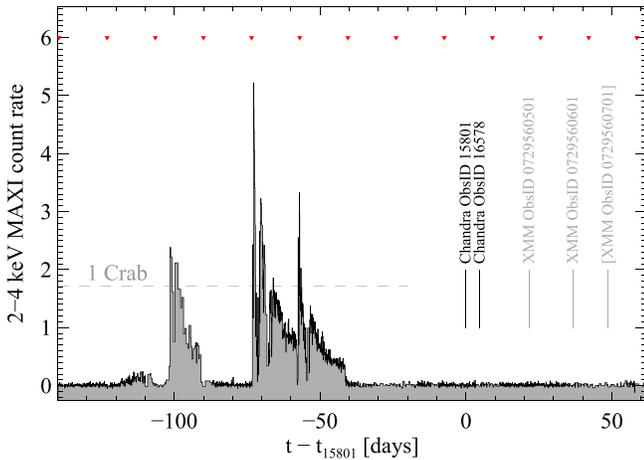


**Figure 3.** MAXI 2–4 keV light curve of Circinus X-1 at the time of the 2013 flare. Also shown are the median-times of our two *Chandra* and three *XMM* observations (*XMM* ObsID 0729560701 was not used in this paper).  $T_0$  was chosen to correspond to the time of our first *Chandra* observation at ( $T_0 = \text{MJD}_{15801} = 56683$ ). Red triangle symbols indicate periastron at orbital phase zero (Nicolson 2007).

rules. The short total exposure time and the fact that the exposures were spread over a time window of 11 days make the *Swift* data unsuitable for the analysis presented in this paper.

### 2.1.1. *Chandra* Observations

In the 3.5 binary orbits preceding the first *Chandra* observation, as well as during the months prior to the flare, the source was quiescent, below the MAXI detection threshold. We observed the source on two occasions with *Chandra*, on 2014 January 25 for 125 ks, and on 2014 January 31 for 55 ks, listed as ObsID 15801 and 16578, respectively. The point source was at very low flux levels during both observations. Circinus X-1 was placed on the ACIS S3 chip.

Data were pipeline processed using CIAO software version 4.6.2. Point sources were identified using the *wavdetect* (Freeman et al. 2002) task and ObsID 16578 was reprojected to match the astrometry of ObsID 15801. For comparison and analysis purposes, we also reprocessed ObsID 10062 (2009) with CIAO 4.6.2 and reprojected it to match the astrometry of ObsID 15801.

We prepared blank background images following the standard CIAO thread (see also Hickox & Markevitch 2006), matching the hard (>10 keV) X-ray spectrum of the background file for each chip.

Figure 4 shows an exposure-corrected, background-subtracted three-color image of the full ACIS field of view (FOV) captured by the observation (ACIS chips 2, 3, 6, 7, and 8 were active during the observation), where red, green, and blue correspond to the 1–2, 2–3, and 3–5 keV bands, respectively. Point sources were identified using *wavdetect* in ObsIDs 10062, 15801, and 16578, source lists were merged and point sources were removed from imaging and spectral analysis. The read streak was removed and the image was smoothed with a  $10''.5$  FWHM Gaussian in all three bands.

The image shows the X-ray binary point source, the X-ray jets (both over-exposed in the center of the image), and the supernova remnant in the central part of the image around the source position at 15:20:40.9,  $-57:10:00.1$  (J2000).

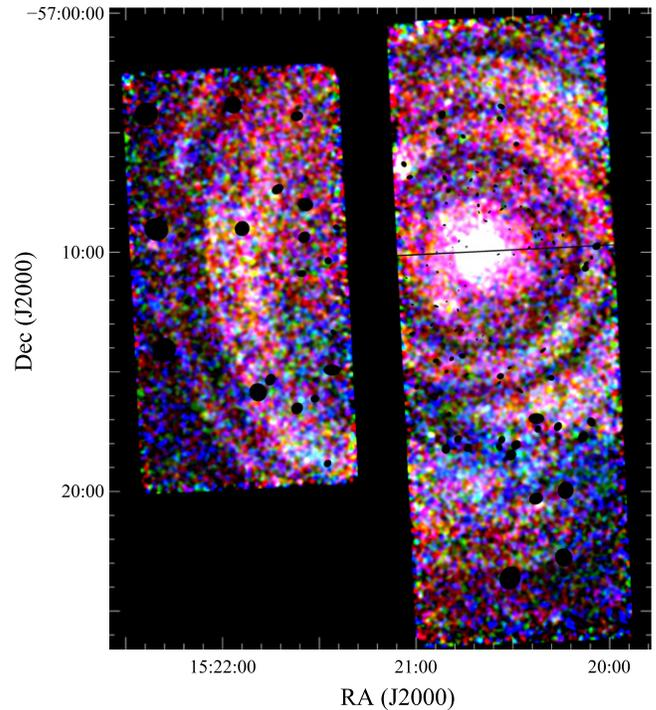


**Figure 4.** Exposure-corrected image of *Chandra* ObsID 15801, smoothed with a  $\text{FWHM} = 10''.5$  Gaussian. Red: 1–2 keV, green: 2–3 keV, blue: 3–5 keV. Point sources and the read streak produced by Circinus X-1 were removed. Four separate rings of dust scattering echoes are visible in this image.

The image also clearly shows at least three bright rings that are concentric on the point source. The first ring spans from 4.2 to 5.7 arcmin in radius, the second ring from 6.1 to 8.2 arcmin, and the third from 8.3 to 11.4 arcmin in radius, predominantly covered by the eastern chips 2 and 3. We will refer to these rings as rings [a]–[c] from the inside out, respectively. An additional ring-like excess is visible at approximately 13 arcmin in radius, which we will refer to as ring [d].

As we will lay out in detail in Section 4, we interpret these rings as the dust-scattering echo from the bright flare in 2013 October–December, with each ring corresponding to a distinct concentration of dust along the line of sight to Circinus X-1. A continuous dust distribution would not produce the distinct, sharp set of rings observed by *Chandra*.

The rings are also clearly visible in ObsID 16578, despite the shorter exposure and the resulting lower signal-to-noise. In ObsID 16578, the rings appear at  $\sim 4\%$  larger radii, consistent with the expectation of a dust echo moving outward in radius (see also Section 3.2 and Equation (10)). The rings are easily discernible by eye in the energy bands from 1 to 5 keV.

Even though the outer rings are not fully covered by the *Chandra* FOV, it is clear that the rings are not uniform in brightness as a function of azimuthal angle. There are clear intensity peaks at [15:21:00,  $-57:06:30$ ] in the inner ring [a] and at [15:20:20,  $-57:16:00$ ] in ring [b] of ObsID 15801. Generally, ring [c] appears brighter on the southeastern side of the image.

The deviation from axisymmetry observed here differs from almost all other observations of dust scattering signatures, which typically appear to be very uniform in azimuth. For example, a detailed investigation of the dust scattering halo of Cygnus X-2 found that the profile deviated by only about 2% from axisymmetry (Seward & Smith 2013). The only comparable observational signature of non-symmetric

scattering features is the light echo off a bok globule observed for Cygnus X-3 (McCullough et al. 2013).

In addition to the light echo, a blue “lane” is visible across the lower part of the image. As we will show below, this feature is the result of photoelectric foreground absorption by an additional layer of dust and gas closer to the observer than the clouds producing the light echo.

### 2.1.2. XMM-Newton Observations

XMM-Newton observed the source on 2014 February 17, (ObsID 0729560501), 2014 March 4, (ObsID 0729560601), and 2014 March 16, (ObsID 0729560701) for 30 ks each. ObsID 0729560501 was not affected by any background flares. The second and third observations were strongly affected by background particle flares, eliminating the use of pn data completely for ObsID 0729560601, and the effective exposure for the MOS detectors after flare rejection was cut to approximately 15 ks in both cases. The resulting data are noisy, suggesting that additional background contamination is present, making the data not usable for detailed, quantitative image processing. We restrict the discussion in this paper to data set 0729560501 (with the exception of Figure 15).

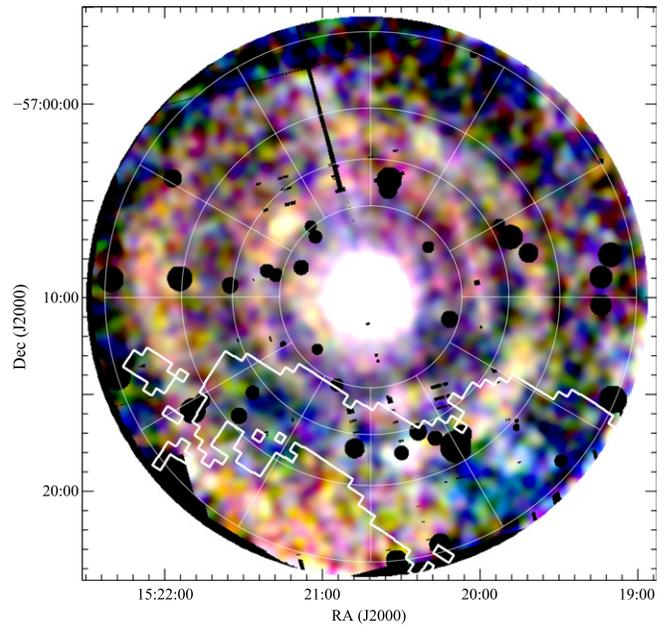
MOS and PN data were reduced using SAS software version 13.5. Data were prepared using the ESAS package, following the standard diffuse source analysis guidelines from the Diffuse Analysis Cookbook.<sup>14</sup> In addition to point sources identified by the ESAS *cheese* task, point sources identified in the three *Chandra* exposures (10062, 15801, 16578) were removed before image and spectral extraction. The energy range from 1.4–1.6 keV around the prominent instrumental aluminum line at 1.5 keV was removed from image processing, while spectral fits determined that the contribution from the Si line at 1.75 keV was sufficiently small to ignore in image processing. Proton and solar-wind charge exchange maps were created using spectral fits to the outer regions of the image and subtracted during image processing.

Figure 5 shows a three color exposure-corrected image of ObsID 0729560501 in the same bands as Figure 4, smoothed with a 35" FWHM Gaussian. Despite the lower spatial resolution of XMM-Newton, the image clearly shows the three rings identified in the *Chandra* images. The median radii of the rings have increased by  $\sim 16\%$  relative to ObsID 15801, corresponding to the longer time delay between the flare and the XMM observation.

Overlaid on the figure is a grid of three annuli covering the rings, broken into twelve angular sections of  $30^\circ$  each. We will use this grid in the discussion below to identify different areas in the image and in corresponding CO maps of the FOV. The rings are labeled [a]–[c] from inside out, and the sections are labeled 1–12 in a clock-wise fashion. See Section 3.1 and Figure 8 for further details on the grid and the nomenclature used in this paper.

### 2.2. CO Data

We used CO data from the Mopra Southern Galactic Plane CO Survey, described in Burton et al. (2013), with the particular data set used here, for the Circinus X-1 region ( $l = 322$ ), coming from the forthcoming public data release in C. Braiding et al. (2015, in preparation). In this data set



**Figure 5.** Exposure-corrected and background-subtracted image of XMM-Newton ObsID 0729560501 (combining EPIC MOS and PN data), smoothed with a FWHM = 35" Gaussian. Colors represent the same energy bands as in Figure 4. Point sources have been removed. The overlaid white-dashed line corresponds to the 15 K km s<sup>-1</sup> contour of the  $-33.6$  to  $-29.6$  km s<sup>-1</sup> <sup>12</sup>CO image shown in Figure 19.

emission from the  $J = 1-0$  line of the three principal isotopologues of the CO molecule (<sup>12</sup>CO, <sup>13</sup>CO, C<sup>18</sup>O, at 115.27, 110.20 and 109.78 GHz, respectively) has been measured at 0.6 arcmin, 0.1 km s<sup>-1</sup> resolution with the 22 m diameter Mopra millimeter wave telescope, located by Siding Spring Observatory in New South Wales in Australia.

By continuously scanning the telescope while making the observations (on-the-fly mapping) large areas of sky can be readily mapped by Mopra. Data cubes covering  $1^\circ \times 1^\circ$  of sky typically take 4 nights with the telescope to obtain, and achieve a  $1\sigma$  sensitivity of about 1.3 and 0.5 K per 0.1 km s<sup>-1</sup> velocity channel for the <sup>12</sup>CO and the (<sup>13</sup>CO, C<sup>18</sup>O) lines, respectively. Such a data cube, covering the G322 region ( $l = 322^\circ - 323^\circ$ ,  $b = -05^\circ$  to  $+05^\circ$ ), was used for the analysis presented here.

### 2.3. 21 cm Data

We use publicly available 21 cm radio data from the Parkes/ATCA Southern Galactic Plane survey (McClure-Griffiths et al. 2005) to estimate the column density of neutral atomic hydrogen toward Circinus X-1. We use CO data to identify velocity components because the velocity dispersion of the H I velocity components is too large to unambiguously resolve individual clouds.

## 3. ANALYSIS

### 3.1. X-Ray Spectral Fits

We performed spectral fits of data from *Chandra* ObsID 15801 and XMM ObsID 0729560501, with results from the spectral analysis presented in Figures 6–9. Because the XMM-Newton FOV is contiguous and covers the rings entirely, we extracted spectra for each ring of XMM ObsID 0729560501 in

<sup>14</sup> <ftp://xmm.esac.esa.int/pub/xmm-esas/xmm-esas.pdf>

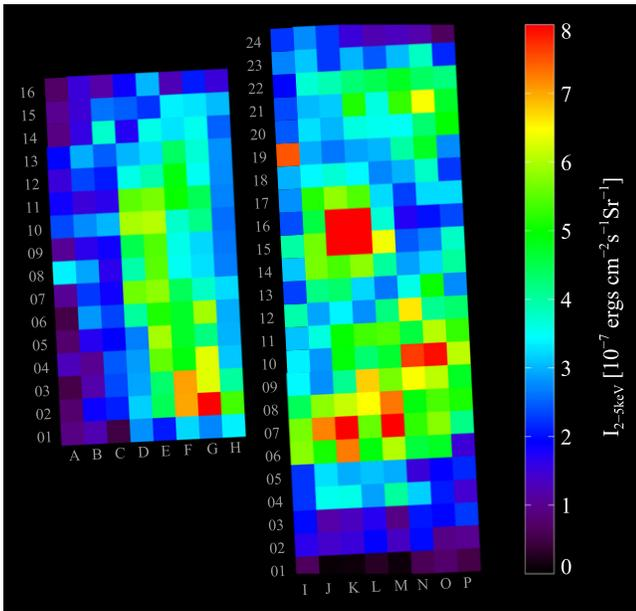


**Figure 6.** Unabsorbed 2–5 keV scattering intensity in units of  $10^{-7} \text{ erg cm}^{-2} \text{ s}^{-1} \text{ Sr}^{-1}$  across the *Chandra* field of view, derived from spectral fits to *Chandra* ObsID 15801 on a rectangular grid of  $8 \times 8$  squares per CCD, labeled by row and column from 1 through 24 and A through P, respectively. photoelectric absorption was removed to isolate the dust-scattered intensity.

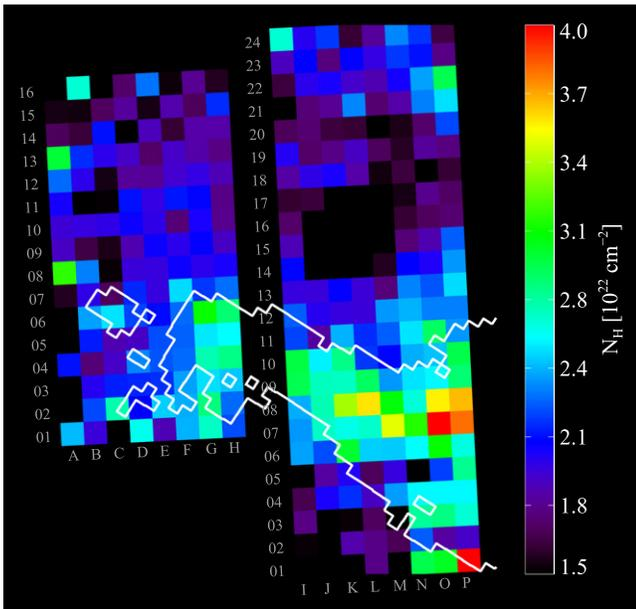


**Figure 7.** Distribution of photoelectric absorption column  $N_{\text{H}}$  derived from the spectral fits shown in Figure 6. A clear excess of absorption is found in the lower half of the image. overlaid is the 15 K  $\text{km s}^{-1}$  contour of the  $-33.6$  to  $-29.6 \text{ km s}^{-1}$   $^{12}\text{CO}$  image shown in Figure 19.

annuli spanning the radial ranges  $[4.7\text{--}7.1, 7.1\text{--}9.7, 9.7\text{--}13.7]$ , with each ring divided into twelve sections. Rings are labeled [a] through [c] (with *lower case* letters denoting *XMM* rings), and the layout of the grid is shown in Figure 8. We divided the *Chandra* FOV into a rectangular grid, with each CCD covered by an  $8 \times 8$  grid of square apertures. The layout of the grid on the ACIS focal plane is shown in Figure 6,

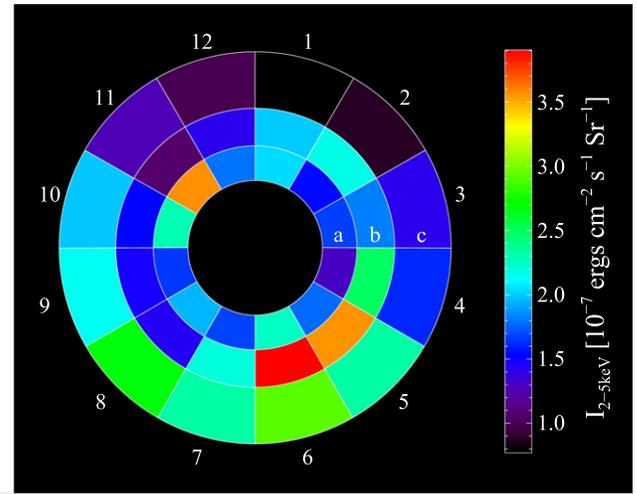


**Figure 8.** Unabsorbed excess 2–5 keV scattering intensity in units of  $\text{erg cm}^{-2} \text{ s}^{-1} \text{ Sr}^{-1}$  across the *XMM* field of view, derived from spectral fits in annular sections identical to those plotted in Figure 5. photoelectric absorption was removed to isolate the dust-scattered intensity. Clear peaks in the surface brightness are located ring sections [a11] and [b6].

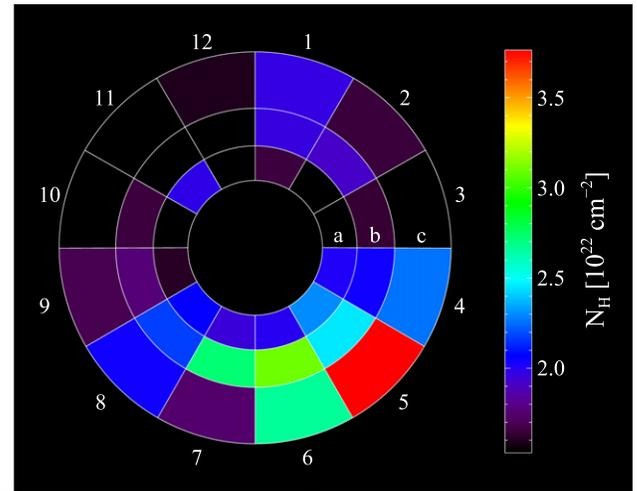


**Figure 9.** Distribution of photoelectric absorption column  $N_{\text{H}}$  derived from the spectral fits shown in Figure 8. A clear excess of absorption is found in the lower half of the image, with a peak at position [c5].

with columns running from [A] through [P] and rows from 1 to 24 (with capital letters denoting *Chandra* columns).

Spectra for *Chandra* ObsID 15801 were generated using the `specextract` script after point source removal. Background spectra were generated from the blank sky background files. No additional background model was required in fitting the *Chandra* data, given the accurate representation of the background in the black sky data.

Spectra for *XMM-Newton* ObsID 0729560501 were extracted from the *XMM-MOS* data using the `ESAS` package and following the Diffuse Analysis Cookbook. In spectral fitting of the *XMM* data, we modeled instrumental features (Al and Si) and solar-wind charge exchange emission by Gaussians with line energies and intensities tied across all spectra and line widths frozen below the spectral resolution limit of *XMM-MOS* at  $\sigma = 1 \text{ eV}$ . We modeled the sky background emission as a sum of an absorbed APEC model and an absorbed power law.

Intensities of both background components were tied across all ring sections.

We modeled the dust scattering emission in each region as an absorbed power law, with floating absorption column and normalization, but with power-law index tied across all regions, with the exception of the tiles covering the central source and the supernova remnant in the *Chandra* image, which span a square aperture from position [J14] to [M18]. Tying the power-law photon index  $\Gamma$  across all spectra is appropriate because (a) the scattering angle varies only moderately across the rings, with

$$\theta_{sc} = \sqrt{\frac{2c\Delta t}{(1-x)xD}} \quad (6)$$

and (b) for the scattering angles considered here ( $\theta_{sc} > 10'$ ), the energy dependence of the scattering cross section is independent of  $\theta_{sc}$ , with  $d\sigma/d\Omega \propto E^{-2}$  (e.g., Draine 2003). While the source spectrum might have varied during the outburst, we are integrating over sufficiently large apertures to average over possible spectral variations.

While the source spectrum during outburst (the echo of which we are observing in the rings) was likely more complicated than a simple power law, we have no direct measurement of the detailed flare spectrum and the quality of the spectra does not warrant additional complications, such as the addition of emission lines which are often present in the spectra when the source is bright (Brandt & Schulz 2000). Dust scattering is expected to steepen the source spectrum by  $\Delta\Gamma = 2$ , and the measured power-law index of

$$\Gamma = 4.00 \pm 0.03 \quad (7)$$

for the scattered emission is consistent with the typically soft spectrum of  $\Gamma \sim 2$  the source displays when in outburst.

The spectral fits resulting from the model are statistically satisfactory, with a reduced chisquare of  $\chi_{\text{red},0729560501}^2 = 839.68/807 \text{ dof} = 1.04$  for the combined fit of the entire set of spectra for ObsID 0729560501 and  $\chi_{\text{red},15801}^2 = 839.68/807 \text{ dof} = 1.05$  for ObsID 15801. We display the *unabsorbed*<sup>15</sup> 2–5 keV intensity maps of *Chandra* ObsID 15801 and *XMM* ObsID 0729560501 in Figures 6 and 8, respectively. The unabsorbed intensity provides a direct measure of the scattering intensity (unaffected by effects of foreground absorption) and is directly proportional to the dust scattering depth. In Figures 7 and 9, we show maps of the photoelectric absorption column density  $N_{\text{H}}$  determined from the spectral fits for *Chandra* ObsID 15801 and *XMM* ObsID 0729560501, respectively.

Four properties of the spectral maps stand out that confirm the qualitative description of the color images in Figures 4 and 5.

1. A clear intensity peak at position [a11] in Figure 8 and [I19] in Figure 6 corresponds to the brightness peaks seen at that position in Figures 4 and 5. The intensity is a factor of two larger than in the neighboring section [a12] in Figure 8, with a similar increment relative to the neighboring sections in Figure 6.
2. There is a clear intensity peak at position [b5] and [b6], with [b6] being approximately two times brighter than

neighboring [b7] in Figure 8. Ring [b] is brighter on the western side of the *XMM* FOV. This peak of ring [b] corresponds to the brightness peak in tiles [L9], [N10], and [O10] in Figure 6.

3. The southern section of ring [c] is brighter than the northern section, with the brightest scattering emission in sections [c5:c8] in Figure 8. Ring [d] overlaps significantly with ring [c], and the color images and intensity maps cannot distinguish the angular distribution of the two rings.
4. There is a clear excess of foreground absorption in the southern sections of the FOV, running from tile [P7] to [B6] in Figure 7. Figure 9 shows the strongest absorption in sections [c5], [b6] and [b7]. This corresponds to the blue absorption lane that runs across the color images in Figures 4 and 5.

The rings clearly deviate from axial symmetry about Circinus X-1, which requires a strong variation in the scattering dust column density across the image. Because the rings are well-defined, sharp features, each ring requires the presence of a spatially well separated, thin distribution of dust (where thin means that the extent of the dust sheet responsible for each ring is significantly smaller than the distance to the source, by at least an order of magnitude).

We present a quantitative analysis of the dust distribution derived from the rings in 3.2, but from simple consideration of the images and spectral maps alone, it is clear that the different dust clouds responsible for the rings have different spatial distributions and cannot be uniform across the *XMM* and *Chandra* FOVs. In particular, the peak of the cloud that produced the innermost ring (ring [a]) must have a strong column density peak in section [a11], while the cloud producing ring [b] must show a strong peak in sections [b5] and [b6]. The excess of photoelectric absorption in the lower half of the image, with a lane of absorption running through the sections [c5], [b6], and [b7], requires a significant amount of *foreground* dust and gas (an excess column of approximately  $N_{\text{H}} \sim 10^{22} \text{ cm}^{-2}$  relative to the rest of the field).

## 3.2. X-Ray Intensity Profiles and Dust Distributions

### 3.2.1. Radial Intensity Profiles

In order to determine quantitatively the dust distribution along the line of sight, we extracted radial intensity profiles of *Chandra* ObsID 10062, 15801, and 16578 in 600 logarithmic radial bins from  $1'$  to  $18.5'$  in the energy bands 1–2, 2–3, and 3–5 keV (after background subtraction and point-source/read-streak removal). We extracted the radial profile of *XMM* ObsID 0729560501 in 300 logarithmic bins over the same range in angles. We subtracted the quiescent radial intensity profile of ObsID 10062 to remove the emission by the supernova remnant and residual background emission.

Because of the variation in photoelectric absorption across the field, we restricted analysis to the 2–5 keV band, which is only moderately affected by absorption. We plot the resulting radial intensity profile of *Chandra* ObsID 15801 in Figure 10. The plot in Figure 10 shows four echo rings labeled [a] through [d] that correspond to the visually identified rings in the previous sections. Several bright sharp peaks in  $I_{2-5 \text{ keV}}(\theta)$  are visible that can also be seen as distinct sharp rings in Figure 4, suggesting very localized dust concentrations. For comparison,

<sup>15</sup> Unabsorbed intensities are calculated from the model fits by removing the effects of photoelectric absorption before determining model fluxes.

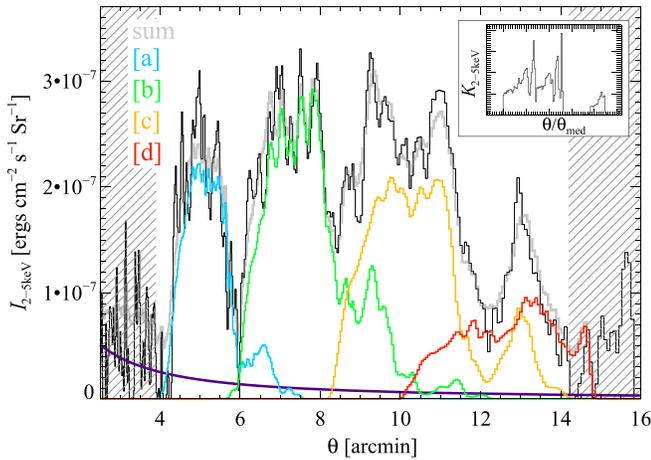


**Figure 10.** Radial X-ray intensity profile of *Chandra* ObsID 15801 in the 2–5 keV band (chosen to roughly match the MAXI 2–4 keV band), shown in black. The intensity profile of *Chandra* ObsID 10062 was subtracted to remove the supernova remnant and residual quiescent background. Overlaid is the full reconstructed radial intensity profile from the deconvolution (gray), as well as the contributions from the four distinct dust concentrations along the line of sight identified in Figure 12 and the power-model of the diffuse instantaneous dust scattering halo (purple line). The hatched area shows the region where the deconvolution becomes unreliable because part of the kernel falls outside of the *Chandra* FOV or onto the supernova remnant. Top right insert: dust scattering kernel  $K(\theta/\theta_{\text{med}})$  (see Equation (9)) used for the deconvolution, derived from the MAXI 2–4 keV light curve during the flare shown in Figure 3, normalized by the total fluence of the outburst.

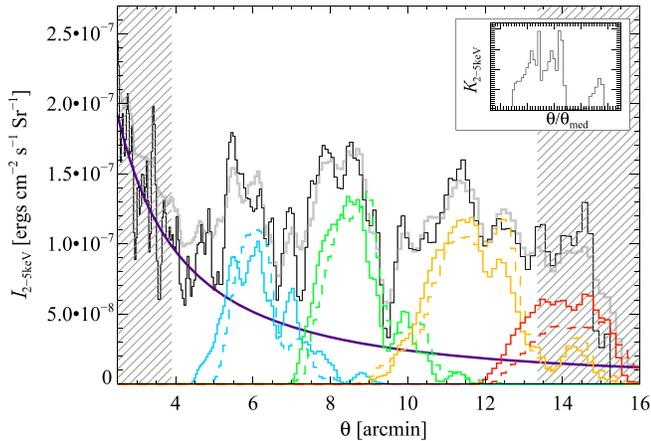


**Figure 11.** Radial X-ray intensity profile of *XMM* ObsID 0729560501 in the 2–5 keV band, following the same labeling and convention as Figure 10. The purple line shows the best-fit power-profile for the instantaneous dust scattering halo (removed before the deconvolution), the colored lines show the contributions from rings [a]–[d] derived from the radial deconvolution of the profile. Overplotted as dashed lines are the radial profiles from rings [a]–[d] predicted by the deconvolution of the *Chandra* ObsID 15801 radial profile. Top right insert: dust scattering kernel  $K(\theta/\theta_{\text{med}})$  (see Equation (9)) used for the deconvolution.

the radial profile of *XMM* ObsID 0729560501 is plotted in Figure 11.

### 3.2.2. Modeling and Removing the Diffuse Instantaneous Dust Scattering Halo

In general, the dust scattering ring echo will be superimposed on the lower-level instantaneous diffuse dust scattering halo produced by the (weak) emission of the point source during and just prior to the observation, which should be removed before analysis of the echo. The 2–5 keV point source

flux during and before ObsID 15801 was very low ( $F_{2-5 \text{ keV}, 15801} \lesssim 6 \times 10^{-12} \text{ erg s}^{-1} \text{ cm}^{-2}$ ), resulting in essentially negligible halo emission, while the two later observations showed larger point source flux ( $F_{2-5 \text{ keV}} \sim 1.8 \times 10^{-11} \text{ erg s}^{-1} \text{ cm}^{-2}$  for ObsID 16578 and  $F \sim 1.3 \times 10^{-11} \text{ erg s}^{-1} \text{ cm}^{-2}$  for 0729560501, with correspondingly brighter diffuse halo emission).

We model the instantaneous dust scattering halo as a power law in ring angle,  $I_{\text{halo}} \propto \theta^\eta$ , appropriate for the large halo angles under consideration and consistent with the steady dust scattering halo profile for Circinus X-1 derived from *Chandra* ObsID 706 in Heinz et al. (2013).

We determine the power-law index to be  $\eta \sim -1.5$  by fitting the intensity profile of ObsID 0729560501 in the radial range between the edge of the supernova remnant at  $\theta > 2.5'$  and the inner edge of ring [a] at  $\theta < 5'$ . This value of  $\eta$  is consistent with the reference dust scattering halo of ObsID 706 from Heinz et al. (2013), which has an index of  $\eta \sim -1.55$  in the 2–5 keV band.

We determine the power-law normalization for ObsID 15801 and 16578 by fits to each radial profile between the outer edge of the remnant at  $\theta > 2.5'$  and the inner edge of ring [a] at  $\theta < 4'$ . We overplot the power-law fits to the instantaneous halo as purple lines in Figures 10 and 11. We subtract the halo emission before further analysis of the ring echo in Sections 3.2.4 and 3.2.5.

### 3.2.3. Deriving the Dust Distribution

Given the well-sampled MAXI light curve of the 2013 flare, we can construct the light echo intensity profile that would be produced by a thin sheet of dust at a given relative dust distance  $x$  and observing time  $t_{\text{obs}}$  from Equations (3) and (4). In general, the different parts of the flare will generate emission at different radii (echoes of earlier emission will appear at larger angles  $\theta$ ).

The scattering angle and thus the scattering cross section will vary for different parts of the light curve, which must be modeled. Given the large scattering angles of  $\theta_{\text{sc}} \gtrsim 1400''$  of the rings and photon energies above 2 keV, it is safe to assume that the cross section is in the large angle limit where  $d\sigma/d\Omega \propto \theta_{\text{sc}}^{-\alpha} \propto \theta^{-\alpha}$  with  $\alpha \sim 4$  (Draine 2003), which we will use in the following. The exact value of  $\alpha$  depends on the unknown grain size distribution. By repeating the analysis process with different values of  $\alpha$ , ranging from 3 to 5, we have verified that our results (in particular, the location of the dust clouds and the distance to Circinus X-1) are not sensitive to the exact value of  $\alpha$ .

For a thin scattering sheet at fractional distance  $x$ , the median ring angle  $\theta_{\text{med}}$  (i.e., the observed angle  $\theta$  for the median time delay  $\Delta t_{\text{med}}$  of the flare) is

$$\theta_{\text{med}} = \sqrt{\frac{2c\Delta t_{\text{med}}(1-x)}{xD}} \quad (8)$$

where  $\Delta t_{\text{med}}$  is a constant set only by the date of the observation and the date range of the flare. The invariant intensity profile  $K_{2-5 \text{ keV}}$  produced by that sheet depends on the observed angle  $\theta$  only through the dimensionless ratio



$z \equiv \theta/\theta_{\text{med}}$ :

$$K_{2-5 \text{ keV}}(z, x) = F_{\text{MAXI}} \left( \Delta t_{\text{med}} z^2 \right) \frac{N_{\text{H},x}}{(1-x)^2} \left. \frac{d\sigma}{d\Omega} \right|_{\theta=\theta_{\text{med}}} z^{-4}. \quad (9)$$

We can therefore decompose the observed radial profile into a series of these contributions from scattering sheets along the line of sight, each of the form  $K_{2-5 \text{ keV}}(\theta/\theta_{\text{med}})$ . Because we chose logarithmic radial bins for the intensity profile, we can achieve this by a simple deconvolution of  $I_{2-5 \text{ keV}}$  with the kernel  $K_{2-5 \text{ keV}}$ . The inset in Figure 10 shows  $K(\theta/\theta_{\text{med}})$  for  $\alpha = 4$ .

### 3.2.4. Deconvolution of the Chandra Radial Profiles

To derive the dust distribution that gave rise to the light echo, we performed a maximum likelihood deconvolution of the *Chandra* radial profiles with this kernel into a set of 600 dust scattering screens along the line of sight. We used the Lucy–Richardson deconvolution algorithm (Richardson 1972; Lucy 1974) implemented in the IDL *ASTROLIB* library.<sup>16</sup> In the region of interest (where the scattering profile is not affected by the chip edge and the supernova remnant), the radial bins are larger than the 50% enclosed energy width of the *Chandra* point-spread function (PSF), such that the emission inside each radial bin is resolved.<sup>17</sup>

Figure 10 shows the reconstructed intensity profile from this distribution for ObsID 15801 (derived by re-convolving the deconvolution with  $K_{2-5 \text{ keV}}$  and adding it to the power-profile for the instantaneous dust scattering halo), which reproduces the observed intensity profile very well, with only minor deviations primarily for rings [a] from 4'–6', while the profile outward of 6' is matched to within the statistical uncertainties.

Figure 12, we plot the inferred dust distribution along the line of sight as a function of median ring angle  $\theta_{\text{med}}$ , derived from our deconvolution of the intensity profile of ObsID 15801, and rebinned onto a uniform grid in  $\theta$ . The plotted quantity is a histogram of the invariant differential scattering depth  $N_{\text{H}}(1-x)^2 d\sigma/d\Omega|_{\theta=\theta_{\text{med}}}$  per bin, which is independent of the distance to Circinus X-1.

The dust distribution clearly shows four main dust concentrations toward Circinus X-1, which we plotted in different colors for clarity. We fit each dust component with a Gaussian to determine the mean location and width, with fit values listed in Table 1. Given the longer median time delay for ObsID 16578, the rings should be observed at larger median angles by a factor of

$$\frac{\theta_{\text{med},16578}}{\theta_{\text{med},15801}} = \sqrt{\frac{\Delta t_{\text{med},16578}}{\Delta t_{\text{med},15801}}} = \sqrt{\frac{6.084 \times 10^6 \text{ s}}{5.628 \times 10^6 \text{ s}}} = 1.04 \quad (10)$$

or 4%, which is consistent with the observed increase in  $\theta_{\text{ring,med}}$ , within the typical width of each cloud.

<sup>16</sup> [http://idlastro.gsfc.nasa.gov/ftp/pro/image/max\\_likelihood.pro](http://idlastro.gsfc.nasa.gov/ftp/pro/image/max_likelihood.pro)

<sup>17</sup> We verified that our results are robust against PSF effects by repeating the deconvolution after smoothing both the profile and the kernel with Gaussians of equal width; this mimicks the effects PSF smearing would have on the deconvolution. The smoothing does not affect our results significantly even for widths an order of magnitude larger than the *Chandra* PSF.

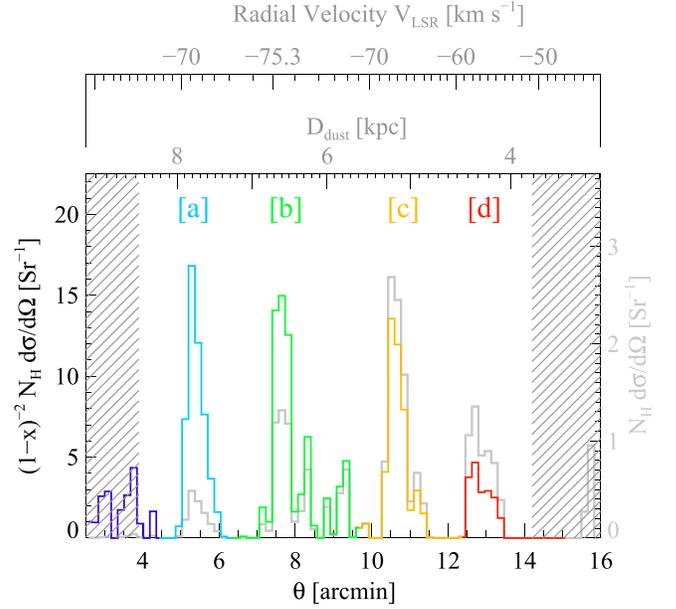


**Figure 12.** Maximum likelihood deconvolution of the 2–5 keV radial intensity profile shown in Figure 10, plotted as a histogram of scattering depth along the line of sight (rebinned onto a uniform grid in  $\theta$ ). Shown in color (left-hand y-axis) is the invariant effective scattering depth  $(1-x)^2 N_{\text{H}} d\sigma/d\Omega$ , where  $x$  is the fractional distance of the dust sheet relative to the distance to Circinus X-1 and  $d\sigma/d\Omega$  is the scattering cross section evaluated at the mean scattering angle of the sheet and at 2 keV. The distribution shows four main components (labeled [a]–[d] in colors blue, green, yellow, and red, respectively). Also shown in gray is the inferred absolute scattering depth  $N_{\text{H}} d\sigma/d\Omega$  for the best-fit distance of  $D_{\text{CirX-1}} = 9.4$  kpc (right-hand y-axis), along with the absolute distance to the scatterer and the associated radial velocity due to Galactic rotation (top axes in gray).

We label the identified dust clouds as components [a]–[d] (plotted in green, blue, yellow, and red, respectively) according to the naming convention adopted above, and identify them with the main X-ray rings seen in the images. To show that this identification is appropriate, we overplot the contribution of each dust cloud to the total intensity profile in the associated color in Figure 10. Rings [a] and [b] are produced primarily by scattering from clouds [a] and [b], while ring [c] and [d] overlap significantly and contain contributions from both clouds.

We tested the uniqueness of the deconvolution procedure using synthetic radial profiles and verified that the procedure faithfully reproduces the dust profile for randomly placed clouds down to a mean flux of about 50% of the background, for counts rates similar to the ones observed in *Chandra* ObsID 15801. Thus, while we cannot rule out the presence of additional weak dust rings below the detection threshold, the identification of the four main dust concentrations producing rings [a]–[d] is robust.

### 3.2.5. Deconvolution of the XMM Radial Profile

The *XMM* data are noisier due to (a) the shorter exposure, (b) the lower scattering intensity given the increased scattering angle at the correspondingly longer time delay, (c) the larger background intensity that is more difficult to model than the stable *Chandra* background, and (d) the brighter dust scattering halo due to the increased point source flux during ObsID 0729560501.

Despite the lower spatial resolution and significantly lower signal-to-noise ratio of the data, the rings are still discernible in

**Table 1**  
Gaussian Fits to Dust Clouds Identified in the Radial Deconvolution in Figure 12

Ring:	$\theta_{\text{med}}$	$\sigma_{\theta}$	$\frac{N_{\text{H}}}{(1-x)^2} \frac{d\sigma}{d\Omega} [\text{S}r^{-1}]^{\text{a}}$	$x^{\text{b}}$
<i>Chandra</i> ObsID 15801				
[a]	5'37 ± 0'02	0'21 ± 0'02	52.56 ± 7.62	0.83
[b]	7'63 ± 0'01	0'19 ± 0'01	47.86 ± 4.77	0.70
[c]	10'64 ± 0'01	0'22 ± 0'01	42.09 ± 3.62	0.55
[d]	12'85 ± 0'04	0'34 ± 0'04	19.60 ± 3.17	0.45
<i>Chandra</i> ObsID 16578				
[a]	5'50 ± 0'02	0'15 ± 0'02	30.25 ± 6.03	0.83
[b]	7'91 ± 0'02	0'20 ± 0'02	36.16 ± 4.18	0.70
[c]	11'10 ± 0'02	0'26 ± 0'02	39.43 ± 3.29	0.55
[d]	13'49 ± 0'02	0'10 ± 0'02	6.51 ± 1.68	0.45
<i>XMM</i> ObsID 0729560501				
[a]	6'00 ± 0'05	0'90 ± 0'06	29.31 ± 2.32	0.84
[b]	8'72 ± 0'02	0'52 ± 0'02	25.56 ± 1.06	0.71
[c]	12'04 ± 0'02	0'73 ± 0'02	23.54 ± 0.92	0.56

**Notes.** Cloud centroids correspond to the median time delay of  $\Delta t_{15801} = 5.628 \times 10^6$  s,  $\Delta t_{16578} = 6.203 \times 10^6$  s, and  $\Delta t_{0729560501} = 7.925 \times 10^6$  s for ObsID 15801, 16578, and 0729560501, respectively. We do not include ring [d] for *XMM* ObsID 0729560501 because its centroid falls outside of the MOS FOV.

<sup>a</sup> Invariant scattering depth, evaluated at the median scattering angle and at 2 keV energy.

<sup>b</sup> Relative distance  $x$  to the dust cloud responsible for the respective ring using the best-fit distance of 9.4 kpc (Equation (13)).

the radial profile in Figure 11. We deconvolved the residual intensity profile following the same procedure used for the *Chandra* data. While the 300 logarithmic radial bins used for the deconvolution are narrower than the 50% enclosed energy width of *XMM*, we verified that the deconvolution was robust by confirming that a strongly smoothed radial intensity profile and/or a smoothed kernel lead to consistent locations and scattering depths within the measurement uncertainties for the dust screens responsible for rings [a]–[c]. The resulting contributions of rings [a] through [d] are overplotted in color in Figure 11, following the same convention as Figure 10.

Gaussian fits to rings [a]–[c] are listed in Table 1. We do not include the fits for ring [d] because its centroid falls too close to the edge of the FOV of *XMM*-MOS at  $\theta \sim 14'.5$  (the *XMM*-PN FOV extends slightly further but is too noisy by itself to reliably extend the profile outward). The inferred relative dust distances agree with the *Chandra* values to better than 5%, indicating that the deconvolution is robust, and consistent with an increase in median ring radius from *Chandra* ObsID 15801 to *XMM* ObsID 0729560501 of  $\sim 16\%$ .

As an additional consistency check, we constructed the radial intensity profile predicted by the deconvolution of the *Chandra* ObsID 15801 radial profile for the increased time delay of *XMM* ObsID 0729560501 (including a decrease in surface brightness by a factor of 1.8 due to the  $\sim 16\%$  larger scattering angle, assuming  $\alpha = 4$ ). The predicted profiles for all four rings are plotted as dashed lines in Figure 11. The profiles of rings [a]–[c] agree well with the *XMM* deconvolution, given (a) the different coverage of the FOV by the

*Chandra* and *XMM* instruments, which should result in moderate differences between the two data sets even if they had been taken at the same time delay and (b) the different angular resolutions and the responses of the telescopes.

### 3.3. CO Spectral and Image Analysis

The deconvolution into dust sheets from Section 3.2 shows that the scattering column density must be concentrated in dense, well localized clouds. Gas with sufficiently high column density (of order  $10^{21}$  cm $^{-2}$ ) and volume number density (of order 100 cm $^{-3}$ ) to produce the observed brightness and arcminute-scale variations in the echo can be expected to be largely in the molecular phase (e.g., Lee et al. 2014).

In order to search for corresponding concentrations of dust and molecular gas, we compared the peaks in the inferred dust column density to maps of CO emission from the Mopra Southern Galactic Plane Survey that cover the entire *Chandra* and *XMM-Newton* FOV.

While CO emission does not directly probe the dust distribution along the line of sight, the largest concentrations of dust will reside in dense molecular gas, and CO is the most easily accessible tracer of molecular gas that includes three-dimensional information about the position of the gas, as well as a measure of the mass of the cold gas through the CO intensity.

The bottom panel of Figure 13 shows the CO spectrum integrated over the entire grid of rings identified in the *XMM-Newton* image in Figure 8, smoothed with a 2 km s $^{-1}$  FWHM Gaussian for noise removal. The spectrum shows five well identified, localized components of molecular gas in the direction of Circinus X-1. A simple multi-Gaussian fit (shown in color in the plot) locates the components at velocities  $v_{\text{LOS},1} = -81$  km s $^{-1}$ ,  $v_{\text{LOS},2} = -73$  km s $^{-1}$ ,  $v_{\text{LOS},3} = -55$  km s $^{-1}$ ,  $v_{\text{LOS},4} = -32$  km s $^{-1}$ , and  $v_{\text{LOS},5} = 9$  km s $^{-1}$ , where component 3 $_{\text{CO}}$  requires two Gaussian components to fit at  $-50$  and  $-55$  km s $^{-1}$ .

While other components of cold gas are likely present below the sensitivity limit of the survey, and while some of the components may be superpositions of several distinct clouds it is clear from the spectrum that these are the primary concentrations of cold gas along the line of sight and therefore the most probable locations of the dust clouds responsible for the observed X-ray light echo.

We adopt the Galactic rotation curve by McClure-Griffiths & Dickey (2007) for the fourth Galactic quadrant within the solar circle. We use the rotation curve by Brand & Blitz (1993) for the outer Galaxy, matched at  $v_{\text{LSR}} = 0$  following the procedure used in Burton et al. (2013), for the Galactic position of Circinus X-1. The resulting radial velocity curve in the direction of Circinus X-1 as a function of distance from the Sun is plotted in the top panel of Figure 13. Because the direction to Circinus X-1 crosses the solar circle, the distance–velocity curve is double-valued, and we cannot simply associate a particular velocity with a given distance.

The rotation curve turns over at a minimum velocity of  $v_{\text{rad}} \geq -75.3$  km s $^{-1}$ . Any velocity component at velocities beyond the minimum *must* be displaced from the Galactic rotation curve and lie near the tangent point. Given the velocity dispersion of molecular clouds of  $\sigma_{\text{CO}} \lesssim 5$  km s $^{-1}$  relative to the LSR (see Section 4), velocities of  $v_{\text{rad}} \gtrsim -80$  km s $^{-1}$ , as measured for component 1 $_{\text{CO}}$  are consistent with the rotation

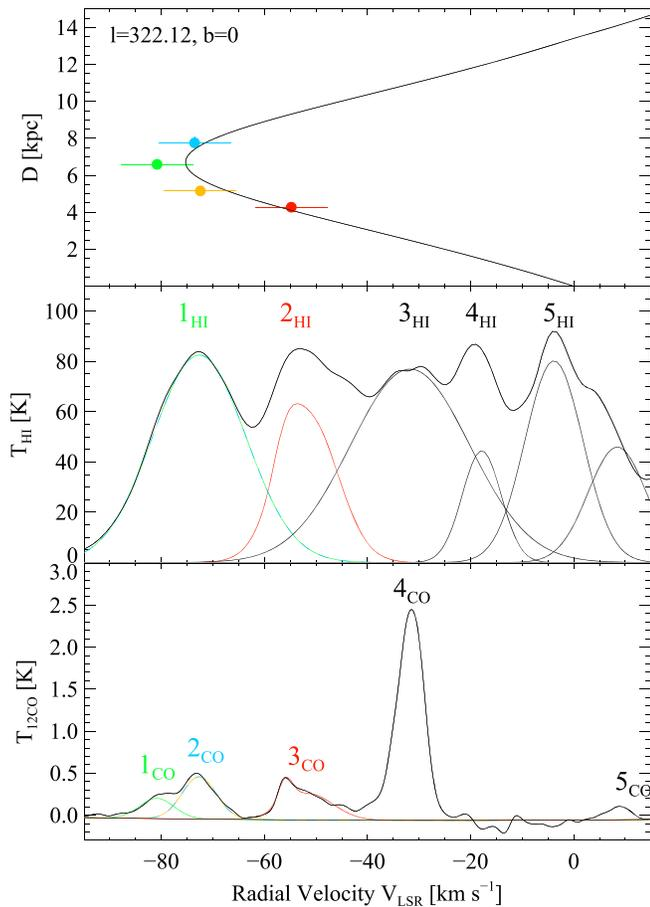


**Figure 13.** Top panel: radial velocity as a function of distance from the Sun for the sight-line in the direction of Circinus X-1 at Galactic coordinates  $l = 322.12$ ,  $b = 0^\circ$ , using the rotation curves from McClure-Griffiths & Dickey (2007) and Brand & Blitz (1993) for the inner and outer Galaxy, respectively. Overplotted are the locations and radial velocities for the four dust clouds [a]–[d] (from top to bottom) responsible for the dust scattering rings, assuming the best-fit distance of 9.4 kpc. Middle panel: 21 cm  $\text{H I}$  spectrum integrated over rings [a]–[c] defined in Figure 8. Component  $1_{\text{HI}}$  comprises CO components  $1_{\text{CO}}$  and  $2_{\text{CO}}$  listed below. Bottom panel:  $^{12}\text{CO}$  spectrum integrated over the same region of rings [a]–[c] from Figure 8, smoothed with a  $2 \text{ km s}^{-1}$  FWHM Gaussian. Five discernible velocity components are labeled  $1_{\text{CO}}$ – $5_{\text{CO}}$ .

curve and place the material at a distance of roughly  $D \sim 6\text{--}8 \text{ kpc}$ .

Given a rotation curve, one could attempt a global distance estimate by simply comparing ring radii and CO velocities. However, a considerably more robust and accurate distance estimate can be derived by also considering the angular distribution of dust inferred from the brightness of each of the rings as a function of azimuthal angle.

### 3.3.1. Differential CO Spectra

In order to identify which cloud is responsible for which ring, we generated adaptively smoothed images of each velocity component within velocity ranges centered on the CO velocity peaks of the clouds. The images are shown in Figures 15–19 and discussed in Section 3.3.2. We also generated CO difference spectra to identify which velocity components may be responsible for the clear brightness enhancements seen in the different rings. They are plotted in Figure 14, which we will discuss below.

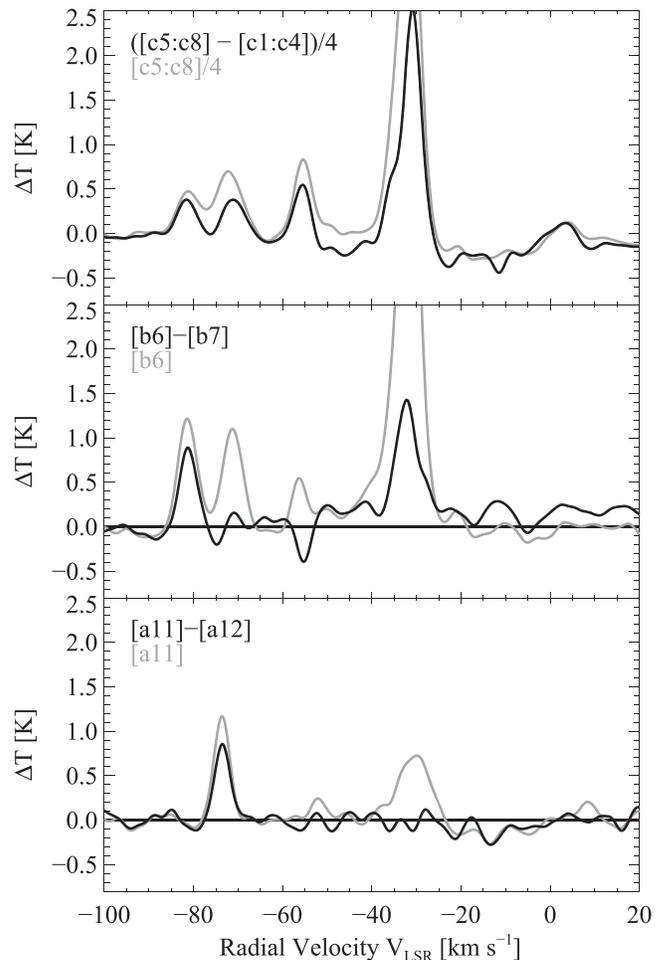


**Figure 14.** Differential (black) and total (gray) Mopra  $^{12}\text{CO}$  spectra of three ring sections (see Figure 8 for a definition of the ring sections), smoothed with a  $3 \text{ km s}^{-1}$  FWHM Gaussian. Differential spectra show comparisons between neighboring ring sections that have large vs. small dust scattering intensity to isolate the CO velocity component responsible for the X-ray peak. Bottom: ring section [a11] minus [a12]; middle: ring section [b6] minus [b7]; top: sum of ring sections [c5:8] minus sum of [c1:4].

The Unabsorbed X-ray intensity shown in Figures 6 and 8 is directly proportional to the scattering dust column density. Variations in  $I_{2-5 \text{ keV}}$  as a function of azimuthal angle therefore probe the spatial distributions of the dust clouds responsible for the different rings. We can use a differential  $^{12}\text{CO}$  spectrum of two ring sections that have significantly different X-ray brightness to identify possible  $^{12}\text{CO}$  velocity components that show a marked difference in column density consistent with the dust enhancement.

The two most obvious regions of strong local variation in  $I_{2-5 \text{ keV}}$  are seen at ring sections [a11] and [b6], both of which are significantly brighter than the neighboring sections [a12] and [b7], respectively.

In the bottom panel of Figure 14, we show the difference  $^{12}\text{CO}$  spectrum of ring sections [a11] minus [a12] (i.e., the spectrum of [a12] subtracted from the spectrum of [a11]) as a black line. We also show the spectrum of [a11] only (i.e., without subtracting [a12]) as a gray line. Because of the strong enhancement in dust detected in [a11], the corresponding CO velocity component must be significantly brighter in [a11] as well, and therefore appear as a positive excess in the difference spectrum. It is clear from the figure that only *one* velocity

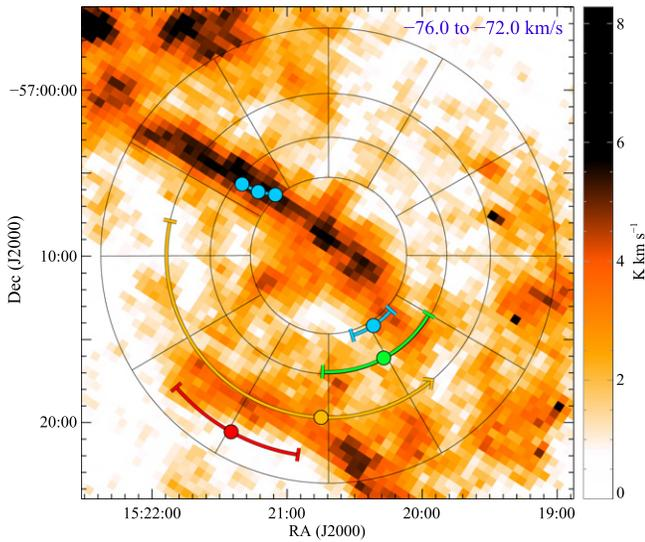


**Figure 15.** Adaptively smoothed Mopra  $^{12}\text{CO}$  image of component  $2_{\text{CO}}$  in the velocity range  $-76$  to  $-72$   $\text{km s}^{-1}$ . The image shows a clear lane of dense molecular gas across the image. Overlaid for comparison is the angular grid used to denote rings in Figure 8. Connected blue dots are the local surface brightness peaks in ring [a11] from *Chandra* ObsID 15801, *XMM* ObsID 0729560501, and *XMM* ObsID 0729560601, showing a clear spatial coincidence with the CO lane. Also overlaid are the centroids (dots) and FWHMs (arcs) of the peaks in the angular intensity distributions of rings [a]–[d] from inside out in blue, green, yellow, and red, respectively, determined from spectral fits to *Chandra* ObsID 15801 in  $10^\circ$  segments for each ring. Note that the arc for ring [a] denotes the secondary peak. The peak of ring [c] is close to the chip edge, indicated by the arrow denoting the lower limit to the ring extent.

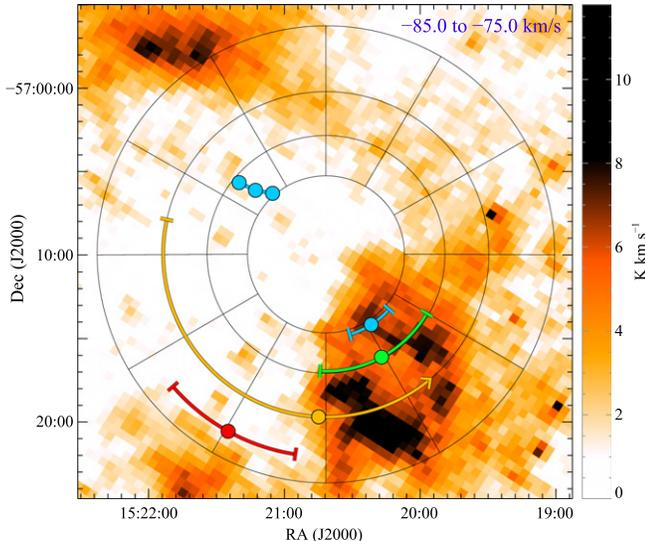


**Figure 16.** Adaptively smoothed Mopra  $^{12}\text{CO}$  image of component  $1_{\text{CO}}$  in the velocity range  $-85$  to  $-75$   $\text{km s}^{-1}$ , with the same nomenclature as in Figure 15. The CO emission in this band shows a clear peak at locations [b5] and [b6], matching the intensity distribution of X-ray ring [b] (green ring segment).

component is significantly enhanced in [a11] relative to [a12], the one at  $v_{\text{rad}} = -74$   $\text{km s}^{-1}$ . We can therefore unequivocally identify velocity component  $2_{\text{CO}}$  at  $-74$   $\text{km s}^{-1}$  as the one responsible for ring [a].

The middle panel of Figure 14 shows the difference  $^{12}\text{CO}$  spectrum of [b6] minus [b7], where the light echo is significantly brighter in [b6] than [b7]. In this case, two  $^{12}\text{CO}$

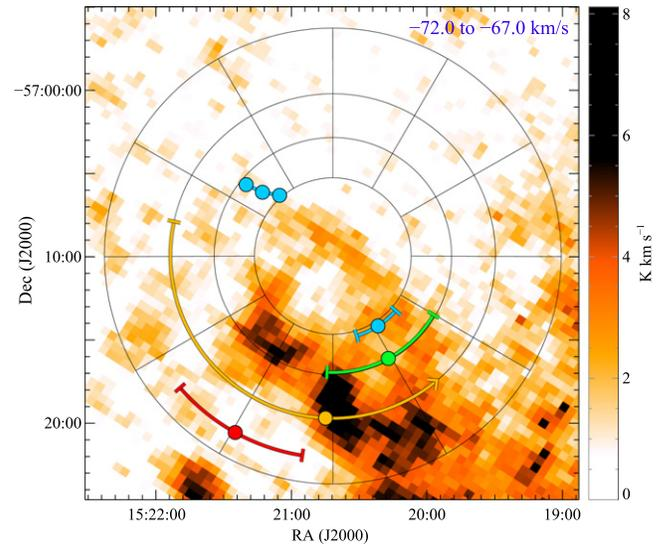


**Figure 17.** Adaptively smoothed Mopra  $^{12}\text{CO}$  image of component  $2_{\text{CO},b}$  in the velocity range  $-72$  to  $-67$   $\text{km s}^{-1}$ , with the same nomenclature as in Figure 15. The CO intensity peak matches the centroid of X-ray ring [c] (yellow arc).

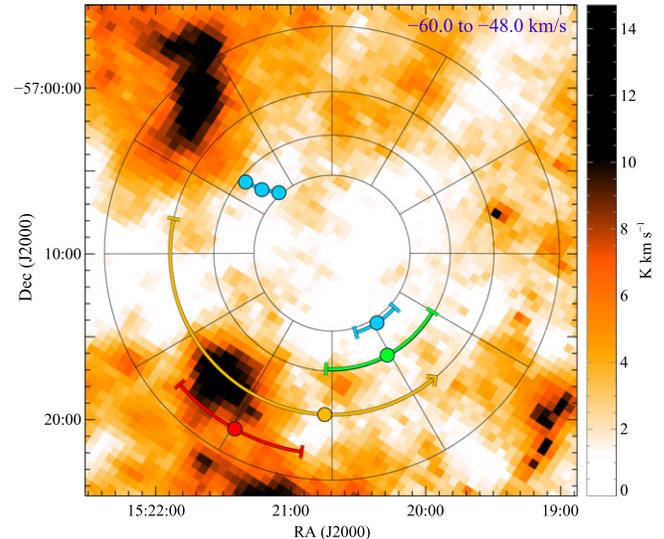


**Figure 18.** Adaptively smoothed Mopra  $^{12}\text{CO}$  image of component  $3_{\text{CO}}$  in the velocity range  $-60$  to  $-48$   $\text{km s}^{-1}$ , with the same nomenclature as in Figure 15. The CO intensity peak in the southern half matches the location of the intensity peak of ring [d] (limited to the *Chandra* FOV; red arc).

velocity components are significantly enhanced in [b6] relatively to [b7], component  $1_{\text{CO}}$  at  $v_{\text{rad}} \sim -80$   $\text{km s}^{-1}$  and component  $4_{\text{CO}}$  at  $v_{\text{rad}} \sim -32$   $\text{km s}^{-1}$ . While we cannot uniquely identify which velocity component is responsible for ring [b] from the spectra alone, we can rule out components  $2_{\text{CO}}$  and  $3_{\text{CO}}$ .

Finally, ring [c] does not show a single clearly X-ray enhanced section relative to neighboring ones. Instead, the southern sections [c5:c8] are significantly enhanced relative to the northern sections [c1:c4]. We therefore plot the difference CO spectrum of sections [c5] through [c8] minus sections [c1] through [c4] (top panel of Figure 14). In this case, all four velocity components are enhanced in [c5:c8] relative to [c1:c4], and we cannot identify even a subset that is responsible for ring [c] from the difference spectrum alone.

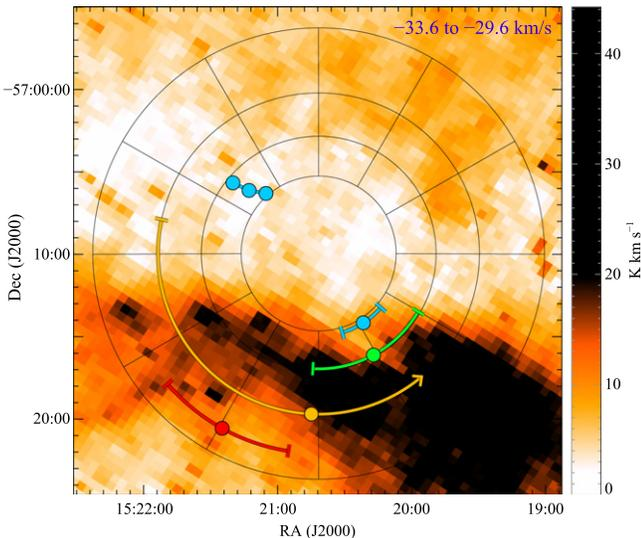


**Figure 19.** Adaptively smoothed Mopra  $^{12}\text{CO}$  image of component  $4_{\text{CO}}$  in the velocity range  $-33.6$  to  $-29.6$   $\text{km s}^{-1}$ , showing the brightest emission feature in the field of view, with the same nomenclature as in Figure 15. The band of molecular gas across the lower half of the image matches the band of absorption seen in the color images in Figures 4 and 5 in position and morphology and corresponds to the excess absorption found in the spectrally determined absorption column shown in Figures 7 and 9.

### 3.3.2. CO Images

In order to compare the ring emission with the spatial distribution of cold gas and dust in the different velocity components identified in Figure 13, we extracted images around the peak of each velocity component, adaptively smoothed to remove noise in velocity channels of low-intensity while maintaining the full Mopra angular resolution in bright velocity channels. We employed a Gaussian spatial smoothing kernel with width  $\sigma = 1.5 \times \{1.0 - 0.9 \exp[-(v - v_{\text{peak}})/(2\sigma_{\text{CO}}^2)]\}$ , where  $v_{\text{peak}}$  and  $\sigma_{\text{CO}}$  are the peak velocity and the dispersion of Gaussian fits to the summed CO spectra shown in Figure 14. This prescription was chosen heuristically to produce sharp yet low-noise images of the different CO clouds.

The CO intensity maps can be compared with the locations of excess X-ray dust scattering to identify potential CO clouds responsible for the different rings, supporting the spectral identification of possible velocity components in Section 3.3.1 and Figure 14. To quantify the deviation of the X-ray rings from axi-symmetry and for comparison with the CO data, we constructed azimuthal intensity profiles of the rings from *Chandra* ObsID 15801 in  $10^\circ$  bins, following the same spectral fitting procedure used to construct Figures 6 and 7. Ring radii in the ranges [a]:  $4' - 6'$ , [b]:  $6' - 8'$ , [c]:  $9' - 10.5'$ , and [d]:  $11.5' - 12.75'$  were chosen to best isolate each ring. The centroids and FWHM of the intensity peaks determined from Gaussian fits for each ring are plotted as colored circles and arcs in Figures 15–19, respectively.

It is important to note that a one-to-one match in the intensity distribution should not be expected on large scales for every ring for three reasons: (a) multiple distinct clouds at *different distances* may fall into the *same* velocity channel because of velocity deviations of the clouds from the local standard of rest; (b) clouds at *different distances* may fall into the *same velocity channel* because of the double-valued nature of the distance–

velocity curve; (c) individual rings may contain scattering contributions from multiple clouds at *different velocities* but *similar distances*.

However, clear local maxima in scattering intensity may be expected to correspond to local maxima in CO emission, and we will base possible cloud-ring identification on local correspondence. Indeed, detailed matches exist for rings [a] and [b], as already expected from the spectra discussed in Section 3.3.1, as well as for ring [d].

- Figure 15 shows an image of CO component  $2_{\text{CO}}$ , integrated over the velocity range  $-76$   $\text{km s}^{-1} < v_{\text{rad}} < -72$   $\text{km s}^{-1}$ , bracketing the velocity component at  $v_{\text{rad}} \sim -74$   $\text{km s}^{-1}$  identified in the differential spectra as giving rise to ring [a]. The clear association of ring [a] with component  $2_{\text{CO}}$  at  $-74$   $\text{km s}^{-1}$  in the CO image is striking. The prominent spectral feature at  $v_{\text{rad}} \sim -74$   $\text{km s}^{-1}$  corresponds to a well-defined lane that runs through the position of Circinus X-1 and crosses ring section [a11]. Overlaid as connected blue circles are the positions of the X-ray surface brightness peaks of ring [a] from *Chandra* ObsID 15801, and *XMM* ObsID 0729560501 and 0729560601 (from inside out, given the increasing ring radius at longer time delays for later observations)<sup>18</sup>. The intensity peak lies exactly on top of the CO peak and traces the CO lane as the rings sweep out larger radii.

The obvious spatial coincidence and the fact that this is the *only* velocity component standing out in the differential spectrum of ring [a11] in Figure 14 *unambiguously* determines that ring [a] must be produced by the dust associated with the CO cloud  $2_{\text{CO}}$  at  $v_{\text{rad}} \sim -74$   $\text{km s}^{-1}$ .

In addition to the narrow lane in the north-eastern quadrant of the image that we identify with the cloud responsible for ring [a], there is an additional concentration of CO emission in this channel in the southern half of the image, which we identify as the cloud likely responsible for at least part of ring [c], and which we discuss further in Figure 17.

This velocity channel straddles the tangent point at minimum velocity  $-75.3$   $\text{km s}^{-1}$  and may contain clouds of the distance range from 5 to 8 kpc (accounting for random motions). It is therefore plausible that multiple distinct clouds may contribute to this image and it is reasonable to associate features in this image with both rings [a] and [c].

- Figure 16 shows the  $^{12}\text{CO}$  image of cloud  $1_{\text{CO}}$  in the velocity range  $-85$   $\text{km s}^{-1} < v_{\text{rad}} < -75$   $\text{km s}^{-1}$ , roughly centered on the peak at  $-81$   $\text{km s}^{-1}$ . The peak of the emission falls into sectors [b5:b6] and [c5:c6], while there is consistent excess CO emission in the eastern part of ring [b]. This spatial coincidence with the observed excess scattering emission of ring [b] strongly suggests that cloud  $1_{\text{CO}}$  is responsible for the bulk of the X-ray scattering for ring [b], consistent with the difference spectrum in the middle panel of Figure 14.

<sup>18</sup> *Chandra* ObsID 16578 is not shown because of the location of the peak at the chip gap and the increased noise at the chip boundary due to the shorter exposure time; *XMM* ObsID 0829560701 is not shown due to the overwhelming noise from the background flare that makes image analysis impossible.

Because of the strong excess foreground absorption in these ring sections (see Figure 9), a direct comparison with the intensity peaks in the X-ray images is more difficult than in the case of ring [a] (because the 3–5 keV channel images are significantly more noisy than the 1–2 and 2–3 keV channels, which are more strongly affected by absorption). However, the clear X-ray intensity peak in sections [b5:b6] denoted by the green arc determined from the spectra correlates well with the peak in CO emission of cloud 1<sub>CO</sub>.

3. Figure 17 shows a low-band image of component 2<sub>CO</sub> in the velocity range  $-72 \text{ km s}^{-1} < v_{\text{rad}} < -67 \text{ km s}^{-1}$ . The CO emission peaks in sections [c5:c7] and corresponds to the centroid in the X-ray intensity of ring [c], which is overplotted as a yellow arc. The good spatial correspondence suggests that ring [c] is produced by a CO cloud at similar velocity but smaller relative distance than the CO cloud responsible for ring [a] shown in Figure 15. Because of the substantial spectral overlap of both clouds, this image may not show the entire extent of the southern part of component 2<sub>CO</sub>.
4. Figure 18 shows an image of cloud 3<sub>CO</sub> in the velocity range  $-60 \text{ km s}^{-1} < v_{\text{rad}} < -48 \text{ km s}^{-1}$ . The CO emission peaks in section [c8], coincident with the peak in the X-ray intensity of ring [d] at the same location (Figure 8). Given the presence of several CO components in the southern half of the image, identification of the intensity peaks of overlapping rings [c] and [d] is not as straightforward. However, it is clear that not all of rings [c] and [d] can be explained by component 3<sub>CO</sub> alone. An additional contribution from material in *other* velocity channels is required to explain the excess emission in section [c5:c6]. Our discussion of Figure 17 suggests that the southern component of 1<sub>CO</sub> is the second component responsible for rings [c] and/or [d].
5. Figure 19 shows an image of cloud 4<sub>CO</sub> in the velocity range  $-33.6 \text{ km s}^{-1} < v_{\text{rad}} < -29.6 \text{ km s}^{-1}$ , which is the dominant CO component in the Mopra FOV. A very bright lane of molecular gas is crossing the southern half of the FOV through sections [c5], [b5:b7]. Comparison with the X-ray images shows a clear spatial overlap of this CO cloud with the bluest sections of the ring emission that we identified as foreground absorption above. A contour of this cloud is overlaid on Figures 5 and 7 and traces the region of highest column density very closely. Because component 4<sub>CO</sub> causes absorption in rings [b]–[d] without a correspondingly large scattering intensity peak (which would have to be about an order of magnitude brighter than the other rings, given the very large column density of component 4<sub>CO</sub>), the main component of cloud 4<sub>CO</sub> must be *in the foreground* relative to the clouds generating the scattering emission of X-ray rings [b]–[d]. The brightest parts of this cloud are almost certainly optically thick in <sup>12</sup>CO. The estimate of the cloud column density for this feature based on the <sup>12</sup>CO intensity in Table 2 is therefore likely an underestimate. In fact, the differential hydrogen column inferred from the X-ray spectra, roughly  $N_{\text{H}} \sim 10^{22} \text{ cm}^{-2}$ , is about a factor of two to three larger than that inferred from <sup>12</sup>CO.

**Table 2**  
Gaussian Fits to CO Velocity Components for Rings [a]–[d]

CO cloud	$v_{\text{CO}} (\text{km s}^{-1})$	$\sigma (\text{km s}^{-1})$	$\frac{N_{\text{H}_2}}{x_{\text{CO},20.3}} (10^{20} \text{ cm}^{-2})^a$
Ring [a]:			
Cloud 2 <sub>CO</sub>	$-73.56 \pm 0.12$	$1.46 \pm 0.12$	$5.09 \pm 0.97$
Ring [b]:			
Cloud 1 <sub>CO</sub>	$-80.85 \pm 0.19$	$2.01 \pm 0.20$	$3.88 \pm 0.97$
Ring [c]:			
Cloud 1 <sub>CO</sub>	$-81.18 \pm 0.15$	$1.72 \pm 0.16$	$2.85 \pm 0.35$
Cloud 2 <sub>CO</sub>	$-72.44 \pm 0.09$	$2.35 \pm 0.09$	$7.71 \pm 0.40$
Cloud 3 <sub>CO</sub>	$-55.39 \pm 0.08$	$1.82 \pm 0.08$	$5.76 \pm 0.34$
Cloud 4 <sub>CO</sub>	$-31.16 \pm 0.02$	$2.16 \pm 0.02$	$36.02 \pm 0.38$
Ring [d]:			
Cloud 1 <sub>CO</sub>	$-81.29 \pm 0.16$	$1.93 \pm 0.17$	$3.43 \pm 0.76$
Cloud 2 <sub>CO</sub>	$-72.14 \pm 0.11$	$2.69 \pm 0.12$	$7.59 \pm 0.90$
Cloud 3 <sub>CO</sub>	$-54.80 \pm 0.09$	$2.26 \pm 0.10$	$7.10 \pm 0.78$
Cloud 4 <sub>CO</sub>	$-30.85 \pm 0.02$	$2.03 \pm 0.02$	$34.22 \pm 0.73$

**Notes.** <sup>12</sup>CO spectra are integrated over rings of radii  $4.0 < R_a < 6.0$ ,  $6.0 < R_b < 8.5$ ,  $8.5 < R_c < 12.0$ , and  $11.0 < R_d < 14.0$ , respectively, weighted by the 3–5 keV *Chandra* intensity. Only velocity components identified in the differential CO spectra plotted in Figure 14 as possible locations of dust responsible for the rings are listed.

<sup>a</sup> hydrogen column density of the velocity component in units of  $10^{20} \text{ cm}^{-2}/x_{\text{CO},20.3}$ , where  $x_{\text{CO},20.3}$  is the CO to H<sub>2</sub> conversion factor in units of the fiducial value  $x_{\text{CO}} = 10^{20.3} \text{ cm}^{-2}/(\text{K km s}^{-1})$  (Bolatto et al. 2013).

From the image comparisons and the differential CO spectra, a clear picture regarding the possible ring–cloud association emerges: Ring [a] must be generated by cloud 2<sub>CO</sub> at  $\sim -74 \text{ km s}^{-1}$ . Ring [b] is generated by cloud 1<sub>CO</sub> at  $\sim -81 \text{ km s}^{-1}$ . At least part of the emission of ring [c] or [d] is likely generated by cloud 3<sub>CO</sub>, but an additional component is required to explain the emission in [c5:c6].

## 4. DISCUSSION

### 4.1. The Distance to Circinus X-1

Based on the ring–cloud association discussed in the previous section, we can use the kinematic distance estimate to each cloud from the <sup>12</sup>CO velocity and the relative distance  $x$  to the cloud from the light echo to constrain the distance to Circinus X-1.

To derive kinematic distances to the clouds, we assume that the molecular clouds measured in our CO spectra generally follow Galactic rotation, with some random dispersion around the LSR. Literature estimates for the value of the 1D velocity dispersion  $\sigma_{\text{cloud}}$  range from  $\sigma_{\text{cloud}} \sim 3.5 \text{ km s}^{-1}$  (Liszt & Burton 1981) for giant molecular clouds in the inner Galaxy to  $7 \text{ km s}^{-1}$  (Stark 1984; Stark & Brand 1989) for moderate-mass high latitude clouds in the solar Galactic neighborhood. Recent studies of kinematic distances to clouds assume a 1D dispersion of  $\sigma_{\text{cloud}} \sim 3 \text{ km s}^{-1}$  around the LSR (e.g., Roman-Duval et al. 2009; Foster et al. 2012). In the following, we will conservatively adopt a value of  $\sigma_{\text{cloud}} \sim 5 \text{ km s}^{-1}$ .

In addition to random cloud motions, an unknown contribution from streaming motions may be present. The magnitude of streaming motions relative to estimates of the Galactic rotation curve is generally relatively poorly constrained observationally (Roman-Duval et al. 2009; Reid et al. 2014). McClure-Griffiths & Dickey (2007) characterized the possible contribution of streaming motions to deviations from the rotation curve in the fourth quadrant and found systematic deviations due to streaming motions with a peak-to-peak amplitude of  $10 \text{ km s}^{-1}$  and a standard deviation of  $\sigma_{\text{streaming}} \sim 5 \text{ km s}^{-1}$ . While streaming motions are not completely random, the four dust clouds responsible for the rings are located at sufficiently different distances that their streaming motions relative to the Galactic rotation curve may be considered as un-correlated. Thus, we will treat the uncertainty associated with streaming motions as statistical and add the dispersion  $\sigma_{\text{streaming}}$  in quadrature to the cloud-to-cloud velocity dispersion, giving an effective 1D bulk velocity dispersion relative to Galactic rotation of  $\sigma_{\text{cloud,eff}} \sim 7 \text{ km s}^{-1}$ .

We assume that the main component of each dust cloud identified in Figure 12 and Table 1 is associated with one of the CO velocity components identified above. However, a single velocity component may be associated with *more* than one ring, given the double-valued nature of the velocity curve and the possible overlap of clouds in velocity space due to excursions from the LSR. For a given distance  $D$  to Circinus X-1, we can then determine the radial velocity of each dust cloud if it were at the LSR, given its relative distance  $x(D, \theta_{\text{med}})$ , and compare it to the observed radial velocities of the CO clouds.

For an accurate comparison, we extracted CO spectra that cover the FOV of *Chandra* ObsIDs 15801 and 16578, limited to the radial ranges [a]:  $4'.0\text{--}6'.0$ , [b]:  $6'.0\text{--}8'.5$ , [c]:  $8'.5\text{--}12'$ , [d]:  $11'.0\text{--}14'.0$  for ObsID 15801 and increase radial ranges by 4% for ObsID 16578 according to Equation (10). We weighted the CO emission across the FOV with the 3–5 keV *Chandra* intensity in order to capture CO emission from the regions of brightest dust scattering. We fitted each identified CO component with a Gaussian and list the relevant CO clouds used in the fits in Table 2.

For a given assumed distance  $D$  to Circinus X-1, we calculate the expected radial velocities of the cloud components and compare them to the observed CO velocities to find the distance that best matches the observed distribution of clouds. We represent each CO cloud  $j$  and each dust cloud  $i$  by the best-fit Gaussians from Tables 1 and 2, respectively, with dispersions  $\sigma_{\text{CO},j}$  and  $\sigma_{\text{dust},i}$  and peak positions  $v_{\text{CO},j}$  and  $v_{\text{dust},i}$ , respectively. In addition, we allow for an effective bulk 1D velocity dispersion of  $\sigma_{\text{cloud,eff}} = 7 \text{ km s}^{-1}$  relative to the Galactic rotation curve as discussed above, comprised of the random cloud-to-cloud velocity dispersion and contributions from streaming motions.

While the velocity distribution of each dust cloud (calculated from the Gaussian fit to the distribution of dust as a function of  $z$ ) is not itself Gaussian, we conservatively use the peak value of the velocity and assign a velocity dispersion  $\sigma_{\text{dust},i}$  that is the larger of the two propagated  $z$ -dispersions in the positive and negative  $z$ -direction from the peak of the cloud.

We combine the measurements on the ring radii from the deconvolutions of ObsID 15801 and 16578, corrected by the expansion factor of the rings given by Equation (10). The goodness of fit is then determined by the likelihood function

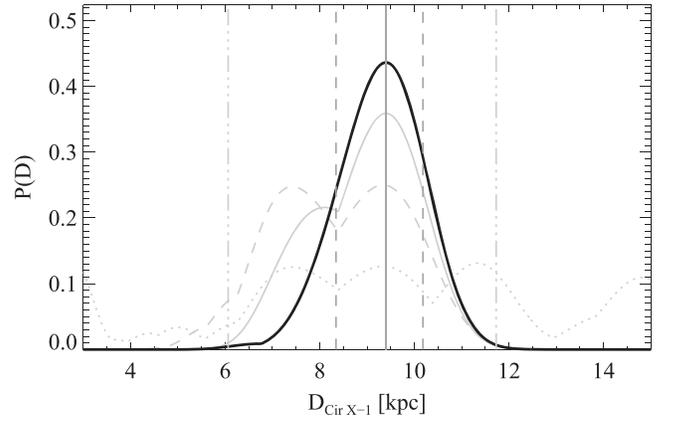


**Figure 20.** Unnormalized posterior of the distance to Circinus X-1 from ObsID 15801 and 16578. Shown in black: likelihood function with all three priors about ring-CO-cloud associations in place (i.e., we identify velocity component  $2_{\text{CO}}$  at  $v_{\text{LOS}} \approx -74 \text{ km s}^{-1}$  with rings [a], component  $1_{\text{CO}}$  at  $v_{\text{LOS}} \approx -80 \text{ km s}^{-1}$  with the peak of ring [b], and require ring [c] and [d] to be produced by different CO components). The likelihood distributions without any priors, with only prior one, and with prior one and two are plotted as dotted, dashed, and solid gray curves, respectively. The most likely distance of 9.4 kpc and the  $1\sigma$  and  $3\sigma$  uncertainties are plotted as solid, dashed, and dashed-triple-dotted gray vertical lines, respectively.

$P(D)$  as a function of distance  $D$ ,

$$P(D) = \frac{1}{N_P} \times \prod_{i=1}^4 \max_{j_i=1}^4 \left\{ \exp \left[ -\frac{\left( v_{\text{dust},i}(D) - v_{\text{CO},j_i} \right)^2}{2 \left( \sigma_{\text{dust},i}^2 + \sigma_{\text{CO},j_i}^2 + \sigma_{\text{cloud}}^2 \right)} \right] \right\} \quad (11)$$

where for each dust cloud  $i$  in the product, the CO component  $j_i$  with the maximum likelihood is chosen from the set of allowed CO components, i.e., the CO component that most closely matches the velocity  $v_{\text{dust},i}$  of dust cloud  $i$ ;  $N_P$  is a normalization factor chosen to ensure that  $\int dD P(D) = 1$ .  $P(D)$  is plotted in Figure 20.

As discussed in Section 3.3.2, we can restrict the CO clouds responsible for the rings based on the visual and spectral identification discussed in Sections 3.3.1 and 3.3.2. We place two strong priors and one weak prior on the association of dust and CO clouds.

1. The first strong prior is the association of ring [a] with CO component  $2_{\text{CO}}$ .
2. The second strong prior is the association of ring [b] with CO component  $1_{\text{CO}}$ .
3. The third, weak prior is the requirement that rings [c] and [d] cannot be produced by component  $3_{\text{CO}}$  alone, i.e., that either ring [c], or ring [d] is associated with a component other than  $3_{\text{CO}}$ .

Functionally, these priors take the form of limits on the possible combinations of rings  $i$  and clouds  $j_i$  in the maximum taken in Equation (11). That is, the first prior eliminates the maximum for ring  $i = 1$  and simply replaces it with the exponential for cloud  $j_i = 2$ , while the second prior replaces the maximum for ring  $i = 2$  with the exponential for  $j_2 = 1$ . The third prior eliminates combinations in the maximum for which  $j = 3$  for both  $i = 3$  and  $i = 4$ .

#### 4.1.1. Distance Estimate with all Three Priors

With all three priors in place, Equation (11) takes the form

$$\begin{aligned}
 P(D) = & \frac{1}{N_p} \\
 & \times \exp \left[ -\frac{(v_{\text{dust},1}(D) - v_{\text{CO},2})^2}{2(\sigma_{\text{dust},1}^2 + \sigma_{\text{CO},2}^2 + \sigma_{\text{cloud,eff}}^2)} \right] \\
 & \times \exp \left[ -\frac{(v_{\text{dust},2}(D) - v_{\text{CO},1})^2}{2(\sigma_{\text{dust},2}^2 + \sigma_{\text{CO},1}^2 + \sigma_{\text{cloud,eff}}^2)} \right] \\
 & \times \prod_{i=3}^4 \max_{j_i=1}^4 \left\{ \left( 1 - \delta_{j_3,3} \delta_{j_4,3} \right) \right. \\
 & \quad \left. \times \exp \left[ -\frac{(v_{\text{dust},i}(D) - v_{\text{CO},j_i})^2}{2(\sigma_{\text{dust},i}^2 + \sigma_{\text{CO},j_i}^2 + \sigma_{\text{cloud,eff}}^2)} \right] \right\} \quad (12)
 \end{aligned}$$

where the product  $\delta_{j_3,3} \delta_{j_4,3}$  of two Kronecker deltas guarantees that rings [c] and [d] cannot both be produced by CO cloud  $j = 3$ , since the term in parentheses vanishes when  $j_3 = j_4 = 3$ .

The likelihood distribution with all three priors in place is shown as a solid black curve in Figure 20. The 68% and 99.7% confidence intervals (corresponding to the one- and three- $\sigma$  uncertainties in the distance to Circinus X-1) are plotted as well.

The best-fit distance to Circinus X-1 with 1- $\sigma$  statistical uncertainties<sup>19</sup> is

$$D_{\text{CirX-1}} = 9.4_{-1.0}^{+0.8} \text{ kpc.} \quad (13)$$

Quantities that depend on  $D_{\text{CirX-1}}$  listed in this paper (such as the relative cloud distance  $x$ ) are calculated using the best-fit value from Equation (13) and are listed in gray color in Table 1 and Figure 12.

The distance listed in Equation (13) is consistent with the dust-cloud associations of rings [a] and [b] with clouds  $2_{\text{CO}}$  and  $1_{\text{CO}}$ , respectively, it places the cloud responsible for rings [c] and [d] at velocities associated with CO components  $2_{\text{CO}}$  and  $3_{\text{CO}}$ , respectively, and it places the CO mass of cloud  $4_{\text{CO}}$  in the foreground of all of the scattering screens, consistent with the observed excess photoelectric absorption observed in the X-ray images that coincides with the location of cloud  $4_{\text{CO}}$ . The locations and velocities to the four scattering screens derived from the best-fit distance are plotted in the top panel of Figure 13, showing that the dust clouds fall close to the Galactic rotation curve.

We overplot the best-fit distance and velocity scale as a function of observed angle  $\theta$  in gray on the top  $x$ -axis in Figure 12. Figure 12 also shows the scattering depth  $N_{\text{H}} d\sigma/d\Omega|_{\text{med}}$  in gray. Because it requires knowledge of  $x(D)$ , this quantity is distance dependent.

The distance derived here is both geometric and kinematic, given that we use kinematic distances to molecular clouds to

<sup>19</sup> Uncertainties in Equation (13) include the effect of random cloud-to-cloud motions and streaming motions as discussed in 4.1. Considering *only* random cloud-to-cloud motions would reduce the uncertainties to  $D_{\text{CirX-1}} = 9.4_{-0.8}^{+0.6}$  kpc, in which case an allowance for a systematic distance error due to streaming motions of order  $\pm 0.5$  kpc (corresponding to a velocity error of  $5 \text{ km s}^{-1}$ ) should be made.

anchor the *absolute* distance scale, and more accurate *relative* geometric distances to the scattering screens. As such, one might refer to this method as either pseudo-kinematic or pseudo-geometric. Given that the predominant error in our method stems from the kinematic aspect of the distance determination, we will simply refer to it as a kinematic distance.

For completeness, we will also list the constraints on the distance with only a subset of priors 1–3 in place:

#### 4.1.2. Distance Estimate with the Two Strong Priors Only

With both priors 1 and 2 in place, a secondary peak appears at 7.8 kpc (solid gray curve in Figure 20), with a  $3\sigma$  lower limit of  $D_{\text{Cir}} > 6.3$  kpc. This peak corresponds to the solutions for which both rings [c] and [d] are produced by cloud  $3_{\text{CO}}$ . The formal  $1\sigma$  uncertainty of the distance to Circinus X-1 from only the two strong priors 1 and 2 is  $D_{\text{CirX-1}} = 9.4_{-1.7}^{+0.8}$  kpc.

#### 4.1.3. Distance Estimate with Only Prior 1 in Place

With only the first prior in place, the likelihood distribution has two roughly equally strong peaks, one at 7.4 kpc and one at 9.4 kpc (dashed gray curve in Figure 20), and the possible distance range is restricted from 4.5 to 11 kpc. The second strong peak at lower distance corresponds to a solution for which both rings [a] and [b] are associated with component  $1_{\text{CO}}$  and rings [c] and [d] are associated with component  $3_{\text{CO}}$ .

#### 4.1.4. Lack of Distance Constraints without any Priors

Without placing *any* priors on dust–CO cloud associations, the source distance is not formally constrained, as can be seen from the dotted curve in Figure 20, which has multiple peaks at distances from 3 to 15 kpc.

### 4.2. Implications of a Distance of 9.4 kpc for the Properties of Circinus X-1

Our three- $\sigma$  lower limit of  $D > 6.1$  kpc on the distance to Circinus X-1 is inconsistent with previous claims of distances around 4 kpc (Iaria et al. 2005). On the other hand, the 1- $\sigma$  distance range listed in Equation (13) is consistent with the distance range of 7.8–10.5 kpc based on the observations of type I X-ray bursts by Jonker & Nelemans (2004), which further strengthens the case for the kinematic distance presented here.

A distance of 9.4 kpc is only marginally larger than the fiducial value of 8 kpc adopted in Heinz et al. (2013). The age of the supernova remnant and thus the age of the X-ray binary increases slightly to  $t_{\text{Cir}} \sim 3000$  years, well within the uncertainties estimated in Heinz et al. (2013), while the supernova energy would increase by about 40%.

At a distance of 9.4 kpc, the X-ray binary itself has exceeded the Eddington luminosity for a 1.4 solar mass neutron star frequently during the time it has been monitored by both the All Sky Monitor on the Rossi X-ray Timing Explorer and MAXI, most recently during the 2013 flare that gave rise to the rings reported here. For example, during the peak of its bright, persistent outburst between about 1995 and 1997, the mean 2–10 keV luminosity of the source was approximately  $L_{1995,2-10 \text{ keV}} \sim 3 \times 10^{38} \text{ erg s}^{-1} (D/9.4 \text{ kpc})^{-2}$ . We estimate the peak flux measured by MAXI during the 2013 flare to be



about 2.2 Crabs, corresponding to a peak luminosity of  $L_{\text{peak},2-10\text{ keV}} \sim 5.6 \times 10^{38} \text{ erg s}^{-1} (D/9.4 \text{ kpc})^{-2}$ .

One of the most intriguing properties of Circinus X-1 is the presence of a powerful jet seen both in radio (Stewart et al. 1993) and X-rays (Heinz et al. 2007). Fender et al. (2004a) reported the detection of a superluminal jet ejection, launched during an X-ray flare. Taken at face value, the observed proper motion of  $\mu \sim 400 \text{ mas day}^{-1}$  at a distance of 9.4 kpc implies an apparent signal speed and jet Lorentz factor of  $\Gamma \gtrsim \beta_{\text{app}} = v_{\text{app}}/c \gtrsim 22 (D/9.4 \text{ kpc})$  and a jet inclination of  $\theta_{\text{jet}} \lesssim 3^\circ (9.4 \text{ kpc}/D)$ . This would make the jet in Circinus X-1 even more extreme than the parameters presented in Fender et al. (2004a), who assumed a fiducial distance of 6.5 kpc.

#### 4.3. The Galactic Positions of Circinus X-1 and Scattering Screens [a]–[d]

At a distance of around 9.4 kpc, Circinus X-1 is likely located inside the far-side of the Scutum–Centaurus arm. A location inside a (star-forming) spiral arm is consistent with the young age of the binary.

The CO cloud nearest to the Sun, component  $4_{\text{CO}}$  at  $\sim -33 \text{ km s}^{-1}$ , is likely located in the near-side of the Scutum–Centaurus arm, explaining the large column density responsible for the foreground absorption.

CO clouds  $1_{\text{CO}}$  through  $3_{\text{CO}}$  are at intermediate distances; association of these clouds with either the Norma arm (or the Scutum–Centaurus arm for cloud  $3_{\text{CO}}$ ) is plausible but difficult to substantiate.

Section 4.1 discussed a possible error due to streaming motions of CO clouds relative to the LSR as part of the large scale Galactic structure. For streaming motions to strongly affect the measured radial velocity to a particular cloud, the cloud would have to be located near a major spiral arm.

The dominant spiral arm toward Circinus X-1 is the near side of the Scutum–Centaurus arm, which crosses the line of sight at roughly 3–4 kpc, which we tentatively identified with cloud  $4_{\text{CO}}$ . CO clouds  $1_{\text{CO}}$  and  $2_{\text{CO}}$ , which dominate the likelihood distribution plotted Figure 20, are likely located far away from the center of that spiral arm. Thus, streaming motions are expected to be moderate (see, e.g., Jones & Dickey 2012 and the artist’s impression of Galactic structure by Benjamin & Hurt,<sup>20</sup> which will limit the deviation of the observed radial velocity of cloud from Galactic rotation. Our error treatment is therefore conservative in including the full velocity dispersion of streaming motions as estimated by McClure-Griffiths & Dickey (2007) for the fourth quadrant.

Given the Galactic rotation curve plotted in Figure 13, the radial velocity corresponding to a distance of 9.4 kpc at the Galactic position of Circinus X-1 is  $v_{\text{LSR}} = -54 \text{ km s}^{-1}$ . Jonker et al. (2007) found a systemic radial velocity of  $v_{\text{rad,Cir}} \sim -26 \pm 3 \text{ km s}^{-1}$ , which would imply a 1D kick velocity of order  $v_{\text{kick,LOS}} \sim 25\text{--}35 \text{ km s}^{-1}$ , consistent with the values inferred for high-mass X-ray binaries in the SMC (Coe 2005) and theoretical expectations for post-supernova center-of-mass velocities of high-mass X-ray binaries (Brandt & Podsiadlowski 1995).

The potential association of Circinus X-1 with the CO velocity component  $5_{\text{CO}}$  at  $v_{\text{LOS}} \approx 9 \text{ km s}^{-1}$  suggested by

<sup>20</sup> [http://solarsystem.nasa.gov/multimedia/gallery/Milky\\_Way\\_Annotated.jpg](http://solarsystem.nasa.gov/multimedia/gallery/Milky_Way_Annotated.jpg)

**Table 3**  
Hydrogen Column Density for Rings [a]–[d] from  $^{12}\text{CO}$  and 21 cm Spectra for *Chandra* ObsID 15801

Ring:	$N_{\text{H}_2} (10^{20} \text{ cm}^{-2})$	$N_{\text{HI}} (10^{20} \text{ cm}^{-2})$	$N_{\text{Htot}} (10^{20} \text{ cm}^{-2})$
[a]	$5.1^{+5.1}_{-2.6}$	$17.1^{+17.6}_{-9.4}$	$27.3^{+20.3}_{-10.7}$
[b]	$3.9^{+3.9}_{-2.0}$	$13.4^{+13.7}_{-7.2}$	$21.2^{+15.7}_{-8.2}$
[c]	$7.7^{+7.7}_{-3.9}$	$32.4^{+32.9}_{-17.1}$	$47.9^{+36.3}_{-18.8}$
[d]	$7.1^{+7.1}_{-3.6}$	$20.6^{+20.6}_{-10.3}$	$34.8^{+25.0}_{-12.5}$

Hawkes et al. (2014) would place Circinus X-1 at the very far end of the allowed distance range and require a very large relative velocity of that cloud with respect to the LSR at more than  $30 \text{ km s}^{-1}$ , both of which would correspond to three- $\sigma$  deviations. We therefore conclude that Circinus X-1 and cloud  $5_{\text{CO}}$  are unassociated.

#### 4.4. Constraints on the Dust Scattering Cross Section

The most robust constraints on the scattering cross section, and thus the properties of the dust responsible for the echo, would be derived by measuring the angular dependence of the brightness of a single ring over time. This is because such a measurement removes the large uncertainty in the total hydrogen column toward a particular cloud, since it would measure the *relative* change in brightness. Unfortunately, because our observations lack the temporal coverage to follow the brightness of each ring over a large range in scattering angle, as done by Tiengo et al. (2010), we cannot probe models of the dust scattering cross section at the same level of detail.

However, we can still place quantitative constraints on  $d\sigma/d\Omega$ , given the scattering depth of the rings shown in Table 1 and estimates of the hydrogen column density in both  $\text{H}_2$  from CO and in neutral hydrogen from the 21 cm data, we can derive constraints on the dust scattering cross section. The scattering angle and the scattering depth depend on  $x(\theta, D)$ , and the ring-cloud associations depend on distance as well.

To derive an estimate of the *molecular* hydrogen column density, we used the values of  $N_{\text{H}_2}$  from Table 3, adopting a value of the CO-to- $\text{H}_2$  conversion factor of  $x_{\text{CO}} = 2 \times 10^{20}$  (Bolatto et al. 2013), allowing for an extra factor of two uncertainty in  $x_{\text{CO}}$ . It should be noted that  $x_{\text{CO}}$  may vary by up to an order of magnitude within individual clouds (Lee et al. 2014).

We estimated the *neutral* hydrogen column density from the 21cm Southern Galactic Plan Survey, following the same extraction regions used to derive the integrated CO intensity: we restricted the extraction region to the *Chandra* FOV and weighted the 21 cm emission by the *Chandra* 3–5 keV surface brightness. We then fitted Gaussian lines to the velocity components, fixing the velocity centroids of the components to the CO velocities listed in Table 2.

Because the 21 cm components are much broader than the CO components, clouds  $1_{\text{CO}}$  and  $2_{\text{CO}}$  are blended in 21 cm emission and we cannot fit them as separate components. To estimate the H I column density in each component, we divide the total column in component  $1_{\text{HI}}$  into two components with a column density ratio given by the ratio of the flux of the CO components  $1_{\text{CO}}$  and  $2_{\text{CO}}$ . We budgeted an additional factor of two uncertainty in the neutral hydrogen column derived from the 21 cm data. The results are listed in Table 3.

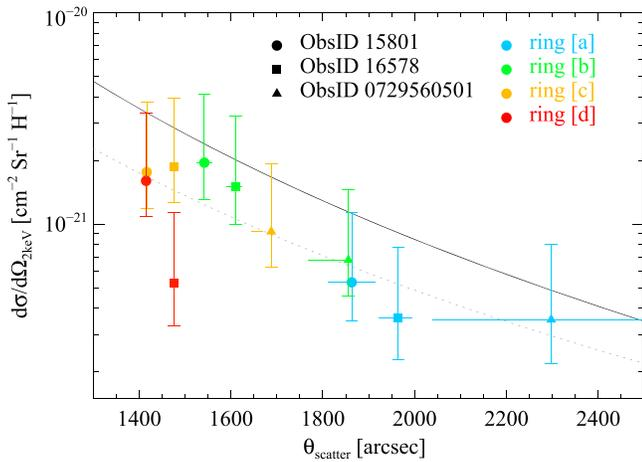


**Figure 21.** Dust scattering cross section as a function of scattering angle, determined from scattering depth (Table 1) and the column density from the measured  $^{12}\text{CO}$  intensity and 21 cm  $\text{H I}$  intensity (Table 3), plotted for *Chandra* ObsID 15801 (circles), ObsID 16578 (squares) and *XMM* ObsID 0729560501 (triangles) for clouds [a]–[d] in green, blue, yellow, and red, respectively, evaluated at energy  $E = 2$  keV. Overplotted is the predicted differential cross section from Draine (2003, solid black line) and the best-fit power law (dotted line). We do not include ring [d] for *XMM* ObsID 0729560501 because its centroid falls outside of the MOS FOV.

Figure 21 shows the differential X-ray scattering cross section  $d\sigma/d\Omega_{\text{sc}}$  per hydrogen atom as a function of scattering angle  $\theta_{\text{sc}}$ , evaluated at 2 keV. Despite the relatively large scatter, the figure shows the expected decline with  $\theta_{\text{sc}}$ . For comparison, the figure shows the scattering cross section derived by Draine (2003), which agrees relatively well with the observations in slope and normalization. Because we associated the entire amount of neutral hydrogen column in the velocity range  $-85$  to  $-30$   $\text{km s}^{-1}$  to the the four clouds, the derived cross sections may be regarded as lower limits, which may be responsible for the vertical offset between model and data.

We also plot the best-fit power law fit to the cross section as a function of  $\theta_{\text{sc}}$  (dotted line):

$$\left. \frac{d\sigma}{d\Omega} \right|_{2 \text{ keV}} \approx (5.8 \pm 2.2) \times 10^{-21} \left( \frac{\theta_{\text{sc}}}{1000'} \right)^{-3.6 \pm 0.7}. \quad (14)$$

It is clear that the large uncertainties in the total hydrogen column dominate the scatter and uncertainty in this plot. Higher resolution 21 cm data would likely improve the accuracy of this plot significantly. Ultimately, a direct correlation of the scattering depth with the absorption optical depth, neither of which depend on the column density of hydrogen, would provide a much cleaner measurement of the scattering cross section. Such an analysis is beyond the scope of this work, however.

#### 4.5. Predictions for Future Light Echoes and the Prospects for X-Ray Tomography of the ISM Toward Circinus X-1

The suitable long-term light curve and the location in the Galactic plane with available high-resolution CO data from the Mopra Southern Galactic Plane Survey make Circinus X-1 an ideal tool to study the properties of dust and its association with molecular gas.

Given our preferred distance to Circinus X-1, we can make clear predictions for observations of future light echoes. Since

the four major rings described in this paper were produced by the molecular clouds associated with the CO velocity components  $1_{\text{CO}}$ ,  $2_{\text{CO}}$ , and  $3_{\text{CO}}$ , future X-ray observations of Circinus X-1 light echoes will show similar sets of rings, with radii for a given time delay determined from Equation (2) and Table 1.

The light echo produced by the CO cloud with the largest column density (cloud  $4_{\text{CO}}$ ) was already outside of the *Chandra* and *XMM* FOVs at the time of the observations. In order to confirm the dust-to-CO-cloud association presented in this paper, future X-ray observations of light echoes should include *Chandra* or *Swift* observations sufficiently close in time to the X-ray flare to observe the very bright light echo expected from cloud  $4_{\text{CO}}$ , which we will refer to as the putative ring [e]. Ring [e] will be brightest in the southern half of the image. Because Circinus X-1 exhibits sporadic flares several times per year, it should be possible to observe this echo with modest exposure times and/or for moderate X-ray fluence of the flare, given the expected large intensity of the echo due to the large column density of cloud  $4_{\text{CO}}$ .

A detection of ring [e] would improve the fidelity of the distance estimate primarily because it would test the ring-cloud-associations assumed in our three priors. However, the statistical improvement on the distance estimate would be marginal because the low relative distance  $x_{4_{\text{CO}}} \sim 0.25$  to cloud  $4_{\text{CO}}$  implies a large change in  $x_{4_{\text{CO}}}$  with  $D$  in such a way that  $D_{4_{\text{CO}}} = x_{4_{\text{CO}}} D$  (and thus also the velocity constraint on cloud  $4_{\text{CO}}$ ) is rather insensitive to  $D$ .

Future observations at smaller delay times will also provide constraints on the scattering cross section at smaller scattering angles. Constraints on  $d\sigma/d\Omega$  from single rings at different scattering angles are inherently less error-prone, as the error in the normalization of  $N_{\text{H}}$  affects all measurement equally, probing the relative change of scattering cross section with  $\theta_{\text{sc}}$ .

Better temporal coverage of the light echo from earlier times will allow detailed maps of each cloud both from the spatial distribution of the scattering signal and from the foreground absorption caused by each of the dust clouds, which can be compared to the scattering depth and the hydrogen column density from CO and  $\text{H I}$  measurements.

Should a high-accuracy distance determination to Circinus X-1 become possible from other methods, (such as maser parallax to one of the CO clouds, in particular cloud  $4_{\text{CO}}$ , which has the highest column density, or VLBI parallax to the source itself), the distance to all dust components will be determined to within 5% accuracy or better (set by the relative angular width  $\sigma_{\text{theta}}/\theta_{\text{med}}$  of the dust cloud from Table 1). This would allow for extremely accurate tomography of the dust and gas distribution toward Circinus X-1 from the existing observations presented here and any future light echo observations, providing a powerful tool to study Galactic structure in the fourth quadrant.

## 5. CONCLUSIONS

The giant flare and the associated X-ray light echo presented in this paper are the brightest and largest set of light-echo rings observed from an X-ray binary to date. The deviation from spherical symmetry allows us to make an unambiguous determination of the clouds responsible for part of the light echo from an X-ray binary.

Because of the full temporal coverage of the light curve of the X-ray flare by MAXI, we are able to reconstruct the dust

distribution toward Circinus X-1 by deconvolving the radial profile with the dust scattering kernel derived from the X-ray light curve.

The kinematic distance of about 9.4 kpc we derived from the association of ring [a] with cloud  $2_{\text{CO}}$  and ring [b] with cloud  $1_{\text{CO}}$  is consistent with the estimate by Jonker & Nelemans (2004) based on the luminosity of the type I X-ray bursts of the source (Tennant et al. 1986). It places a large cloud of molecular gas (cloud  $4_{\text{CO}}$  and the associated large absorption column in the southern quadrant of the FOV) in the foreground of the dust screens detected in the light echo.

At a distance of about 9.4 kpc the source has exceeded the Eddington limit for a  $1.4 M_{\odot}$  neutron star frequently during the time it has been monitored by the All Sky Monitors on the *Ross X-ray Timing Explorer* and MAXI, both during recent outbursts and, more importantly, in average luminosity during its persistent high-state in the 1990s.

Taken at face value, the observed pattern speeds in the jet (Fender et al. 2004b) indicate a very fast jet speed of  $\Gamma \gtrsim 22$  and a correspondingly small viewing angle of  $\theta_{\text{jet}} \lesssim 3^{\circ}$ .

Future measurements of light echoes from Circinus X-1 will allow accurate measurements of the dust scattering cross section as a function of scattering angle and an estimation of the dust-to-gas ratio in the different clouds identified in the FOV toward Circinus X-1.

The technique used to derive the kinematic distance to Circinus X-1 holds significant promise for future observations of light echoes from X-ray transients.

We would like to thank Snezana Stanimirovic, Bob Benjamin, Audra Hernandez, Min-Yong Lee, and Eugene Churazov for helpful discussions. We would also like to thank the CXC team for outstanding support in scheduling and analyzing the *Chandra* observations. This research has made use of data obtained from the *Chandra* Data Archive and the *Chandra* Source Catalog, and software provided by the *Chandra* X-ray Center (CXC) in the application packages CIAO, ChIPS, and Sherpa. Support for this work was provided by the National Aeronautics and Space Administration through *Chandra* Award Number GO4-15049X issued by the *Chandra* X-ray Observatory Center, which is operated by the Smithsonian Astrophysical Observatory for and on behalf of the National Aeronautics Space Administration under contract NAS8-03060. *XMM* data used in this manuscript were obtained through generously scheduled Director's Discretionary Time. This work is based on observations obtained with *XMM-Newton*, an ESA science mission with instruments and contributions directly funded by ESA Member States and the USA (NASA). During the preparation of this manuscript, we made use of the *XMM-ESAS* package. We would like to thank the *Swift* scheduling team for help in planning and executing this program. The CO data was obtained using the Mopra radio telescope, a part of the Australia Telescope National Facility which is funded by the Commonwealth of Australia for operation as a National Facility managed by CSIRO. The University of New South Wales (UNSW) digital filter bank (the UNSW-MOPS) used for the observations with Mopra was

provided with support from the Australian Research Council (ARC), UNSW, Sydney and Monash Universities, as well as the CSIRO. This research has made use of the MAXI data provided by RIKEN, JAXA and the MAXI team. We acknowledge the use of public data from the *Swift* data archive.

## REFERENCES

- Asai, K., Mihara, T., Matsuoka, M., et al. 2014, *PASJ*, **66**, 79  
 Bolatto, A. D., Wolfire, M., & Leroy, A. K. 2013, *ARA&A*, **51**, 207  
 Brand, J., & Blitz, L. 1993, *A&A*, **275**, 67  
 Brandt, N., & Podsiadlowski, P. 1995, *MNRAS*, **274**, 461  
 Brandt, W. N., & Schulz, N. S. 2000, *ApJL*, **544**, L123  
 Burton, M. G., Braiding, C., Glueck, C., et al. 2013, *PASA*, **30**, 44  
 Calvelo, D. E., Fender, R. P., Tzioumis, A. K., et al. 2012, *MNRAS*, **419**, 436  
 Clarkson, W. I., Charles, P. A., & Onyett, N. 2004, *MNRAS*, **348**, 458  
 Coe, M. J. 2005, *MNRAS*, **358**, 1379  
 Corrales, L., & Paerels, F. 2013, arXiv:1311.55  
 Draine, B. T. 2003, *ApJ*, **598**, 1026  
 Fender, R., Wu, K., Johnston, H., et al. 2004a, *Natur*, **427**, 222  
 Fender, R. P., Belloni, T. M., & Gallo, E. 2004b, *MNRAS*, **355**, 1105  
 Foster, J. B., Stead, J. J., Benjamin, R. A., Hoare, M. G., & Jackson, J. M. 2012, *ApJ*, **751**, 157  
 Freeman, P. E., Kashyap, V., Rosner, R., & Lamb, D. Q. 2002, *ApJS*, **138**, 185  
 Hawkes, J., Rowell, G., Dawson, B., et al. 2014, *IJMPS*, **28**, 60198  
 Heinz, S., Schulz, N. S., Brandt, W. N., & Galloway, D. K. 2007, *ApJL*, **663**, L93  
 Heinz, S., Sell, P., Fender, R. P., et al. 2013, *ApJ*, **779**, 171  
 Hickox, R. C., & Markevitch, M. 2006, *ApJ*, **645**, 95  
 Iaria, R., Spanò, M., Di Salvo, T., et al. 2005, *ApJ*, **619**, 503  
 Jones, C., & Dickey, J. M. 2012, *ApJ*, **753**, 62  
 Jonker, P. G., & Nelemans, G. 2004, *MNRAS*, **354**, 355  
 Jonker, P. G., Nelemans, G., & Bassa, C. G. 2007, *MNRAS*, **374**, 999  
 Lee, M.-Y., Stanimirović, S., Wolfire, M. G., et al. 2014, *ApJ*, **784**, 80  
 Linares, M., Watts, A., Altamirano, D., et al. 2010, *ApJL*, **719**, L84  
 Liszt, H. S., & Burton, W. B. 1981, *ApJ*, **243**, 778  
 Lucy, L. B. 1974, *AJ*, **79**, 745  
 Mao, J., Ling, Z., & Zhang, S.-N. 2014, *ApJ*, **785**, 23  
 Mathis, J. S., & Lee, C.-W. 1991, *ApJ*, **376**, 490  
 Matsuoka, M., Kawasaki, K., Ueno, S., et al. 2009, *PASJ*, **61**, 999  
 McClure-Griffiths, N. M., & Dickey, J. M. 2007, *ApJ*, **671**, 427  
 McClure-Griffiths, N. M., Dickey, J. M., Gaensler, B. M., et al. 2005, *ApJS*, **158**, 178  
 McCollough, M. L., Smith, R. K., & Valencic, L. A. 2013, *ApJ*, **762**, 2  
 Nicolson, G. D. 2007, *ATel*, **985**, 1  
 Oosterbroek, T., van der Klis, M., Kuulkers, E., van Paradijs, J., & Lewin, W. H. G. 1995, *A&A*, **297**, 141  
 Parkinson, P. M. S., Tournear, D. M., Bloom, E. D., et al. 2003, *ApJ*, **595**, 333  
 Predehl, P., & Schmitt, J. H. M. M. 1995, *A&A*, **293**, 889  
 Reid, M. J., Menten, K. M., Brunthaler, A., et al. 2014, *ApJ*, **783**, 130  
 Richardson, W. H. 1972, *JOSA*, **62**, 55  
 Roman-Duval, J., Jackson, J. M., Heyer, M., et al. 2009, *ApJ*, **699**, 1153  
 Sell, P. H., Heinz, S., Calvelo, D. E., et al. 2010, *ApJL*, **719**, L194  
 Seward, F. D., & Smith, R. K. 2013, *ApJ*, **769**, 17  
 Shirey, R. E., Bradt, H. V., Levine, A. M., & Morgan, E. H. 1996, *ApJL*, **469**, L21  
 Soleri, P., Heinz, S., Fender, R., et al. 2009, *MNRAS*, **397**, L1  
 Stark, A. A. 1984, *ApJ*, **281**, 624  
 Stark, A. A., & Brand, J. 1989, *ApJ*, **339**, 763  
 Stewart, R. T., Caswell, J. L., Haynes, R. F., & Nelson, G. J. 1993, *MNRAS*, **261**, 593  
 Stewart, R. T., Nelson, G. J., Penninx, W., et al. 1991, *MNRAS*, **253**, 212  
 Svirski, G., Nakar, E., & Ofek, E. O. 2011, *MNRAS*, **415**, 2485  
 Tennant, A. F., Fabian, A. C., & Shafer, R. A. 1986, *MNRAS*, **221**, 27P  
 Tiengo, A., Vianello, G., Esposito, P., et al. 2010, *ApJ*, **710**, 227  
 Tudose, V., Fender, R. P., Kaiser, C. R., et al. 2006, *MNRAS*, **372**, 417  
 Vianello, G., Tiengo, A., & Mereghetti, S. 2007, *A&A*, **473**, 423  
 Xiang, J., Lee, J. C., Nowak, M. A., & Wilms, J. 2011, *ApJ*, **738**, 78